UNIVERSITY OF CALIFORNIA,
IRVINE

Three-Dimensional CT-based Dynamic Elastography of Tissues and Materials

THESIS

submitted in partial satisfaction of the requirements
for the degree of

MASTER OF SCIENCE

in Civil Engineering

by

Lei Jia

Thesis Committee:
Professor Lizhi Sun, Chair
Professor Mo Li
Associate Professor Mohammad Javad Abdolhosseini Qomi

2023

DEDICATION

To my parents' support and my wife Jinjuan's understanding, and the people who advise me, and support me all the time.

TABLE OF CONTENTS

LIST OF FIGURES

LIST OF TABLES

ACKNOWLEDGEMENTS

I would like to express my deepest appreciation to my committee chair, Professor Lizhi Sun, whose extraordinary blend of genius and enthusiasm for research and teaching has profoundly shaped my academic journey. His unwavering support and insightful guidance have been the cornerstone of this dissertation.

I would like to thank my committee members, Professor Mo Li and Professor Mohammad Javad Abdolhosseini Qomi, who gave me a strong interest in studying materials and structural science.

I would like to thank my family and friends for their unconditional support and understanding.

ABSTRACT OF THE THESIS

Three-Dimensional CT-based Dynamic Elastography of Tissues and Materials

by

Lei Jia

Master of Science in Civil Engineering

University of California, Irvine, 2023

Professor Lizhi Sun, Chair

Elastography has emerged as a groundbreaking technique in recent decades, playing a pivotal role in enhancing medical imaging, especially in the realms of ultrasound diagnostics and magnetic resonance imaging. This research study delved deeply into these applications, distilling core procedures, effective methodologies, and universal computational strategies. It represents a pivotal advancement in proposing CT-based Dynamic Elastography (CTDE), establishing the theoretical and practical framework for its study and application.

Venturing further, this research conducted meticulous virtual experiments to validate hypotheses and methodologies in CT-based elastography. This study utilized the finite element method to conduct simulations, which can obtain the same results as real-world dynamic vibration and CT-based imaging. Through analyzing CT data, the infinitesimal displacement generated as mechanical waves propagate through various tissues and materials can be measured, thereby determining the elasticity map.

The two-dimensional simulations yielded a clear modulus map, not only affirming the proposed CTDE method but also laying a solid foundation for three-dimensional exploration. In

the realm of three-dimensional experiments, we utilized CT imaging data, from which both displacement and modulus maps were generated upon processing. Our analysis revealed that this elastography technique refines the contours within CT images, supplementing them with comprehensive modulus data, and thus equips physicians with an advanced diagnostic tool for the precise identification of potential tissue anomalies. Looking forward, the prospects of CT elastography hold significant promise, indicative of a forthcoming era in advanced medical imaging that could revolutionize both research and clinical practice.

Chapter 1. Introduction

1.1 Background

It is widely known that the hardness of pathological areas in the human body can be various. Thus, by identifying differences in hardness, one can determine the depth of the disease. Take breast cancer as an example, which is the most common cancer among women in the United States. It accounts for approximately 30% of all new female cancer cases annually [1]. The following is a comparison of Young's modulus values between breast cancer and normal human tissues. Notably, the elastic modulus of ductal carcinoma in the breast is higher, as shown in Figure 1 [2]. Therefore, for the diagnosis of breast cancer, a physical examination is usually conducted to check for the presence of lumps or swelling by press. However, bumps that can be felt are usually larger and superficial. Quantitative evaluation of the hardness and size of lesions in deeper regions is challenging.

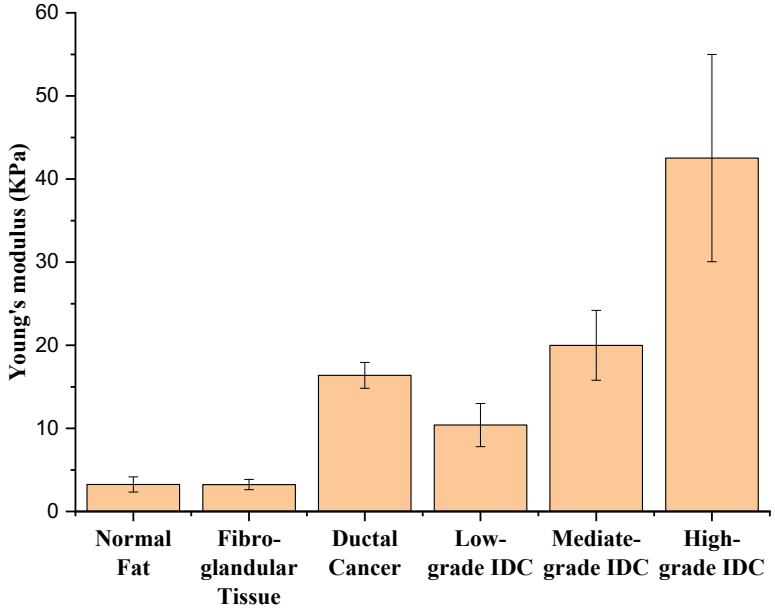

Figure 1. Comparison data come from [2]. Young's modulus values of breast cancer and normal human tissues

To quantitatively visualize the hardness of pathological sites, I have delved into the development of ultrasound imaging and magnetic resonance imaging (MRI). The primary method of obtaining elastography is by applying shear waves to calculate the shear modulus. J. Ophir and colleagues conducted a quantitative analysis imaging of the strain and elastic modulus distribution in soft tissues using ultrasound, achieving excellent resolution [3]. R. Muthupillai and others obtained the shear modulus in gel materials through MRI technology. They were able to efficiently measure the displacement patterns corresponding to the cyclic displacements of small particles, highlighting their potential for medical tissue elastography [4]. Today, both ultrasound elastography and magnetic resonance elastography (MRE) techniques have been applied in clinical trials.

There have been few studies reported in the field of X-ray elastography. Research by Theron J. Hamilton and others, which simultaneously used ultrasound and X-rays, highlighted the feasibility and potential of X-ray elastography [5]. Chika Kamezawa and colleagues conducted dynamic X-ray elastography following the application of shear waves [6]. It is precisely these studies that demonstrate the potential of X-rays in the field of elastography, due to their higher spatial resolution, allowing for the detection of deeper and smaller lesions.

1.2 Selection of Diagnostic Tools

Ultrasound elastography and MRE have already been utilized clinically. B.S. Garra and colleagues differentiated benign from malignant lumps using ultrasound elastography [7]. Rohit Loomba and others employed MRE to predict advanced fibrosis in patients with non-alcoholic fatty liver disease [8]. Yogesh K. Mariappan and colleagues found that the precision of X-ray elastography surpasses both ultrasound elastography and MRE, as shown in Figure 2 [9]. Given its superior spatial resolution and greater imaging depth, research into X-ray elastography

becomes highly significant. This paper concludes the experience of X-ray elastography, and how it can be achieved, and delves into the potential of CT elastography, and the method of using CT for elastography.

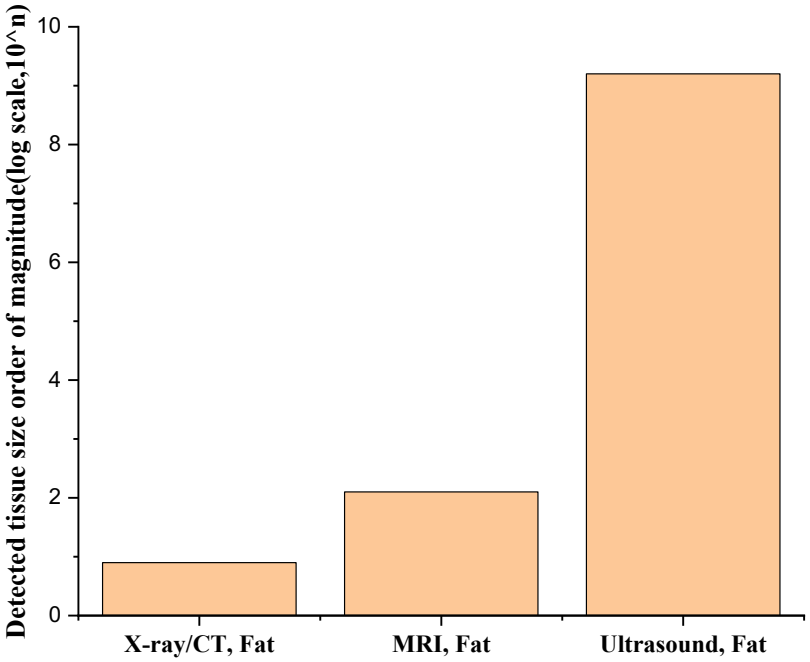

Figure 2. Comparison data come from [9]. Detected tissue size order of magnitude between X-ray/CT, MRI, and Ultrasound

X-rays, discovered in 1895 by Wilhelm Conrad Röntgen, are a form of electromagnetic radiation. They possess the ability to penetrate various materials, including the human body, to varying degrees. This differential absorption allows the visualization of internal structures, such as bones and certain organs, thereby providing invaluable diagnostic information [10]. Traditional X-ray imaging, or radiography, produces two-dimensional (2D) images, which can be limited in detailing complex anatomic regions due to overlapping structures.

Computed Tomography (CT), developed in the 1970s, revolutionized medical imaging by producing cross-sectional images, or "slices", of the body. This is achieved by rotating the X-ray source and detectors around the patient, capturing multiple projections that are then

reconstructed into a detailed image using computational algorithms. The advantage of CT over traditional X-rays is its ability to image complex anatomies without overlap, offering superior contrast resolution. This enables clearer visualization of soft tissues, blood vessels, and other intricate structures, making it a vital tool in various medical specialties [11].

Leveraging X-ray-based elastography research offers the flexibility to analyze tissues not only in a two-dimensional space but also extends the capability to a three-dimensional realm. This multidimensional approach provides a more comprehensive visualization of tissue structures and their elastic properties, thereby enhancing our understanding of their biomechanical behavior. The potential of transitioning from two-dimensional to three-dimensional (3D) imaging could revolutionize diagnostics by providing a depth-resolved analysis of tissue mechanics and pathology.

Chapter 2. Literature Review of Methods of Elastography

2.1 Theoretical Foundations of Elastography

Elastography is a non-invasive technique utilized in imaging to evaluate the mechanical characteristics of tissues. It encompasses the determination of tissue deformation arising from applied mechanical stress, and thereafter calculating the tissue's elastic modulus or rigidity. Alterations in the elastic modulus frequently occur due to pathological transformations within the tissues. Determining these variations enables healthcare practitioners to understand anomalies better and potentially pinpoint their root causes. We have examined literature on ultrasonic elastography, MRI elastography, and existing X-ray elastography, and have summarized the methods map of elastography, as shown in Figure 3.

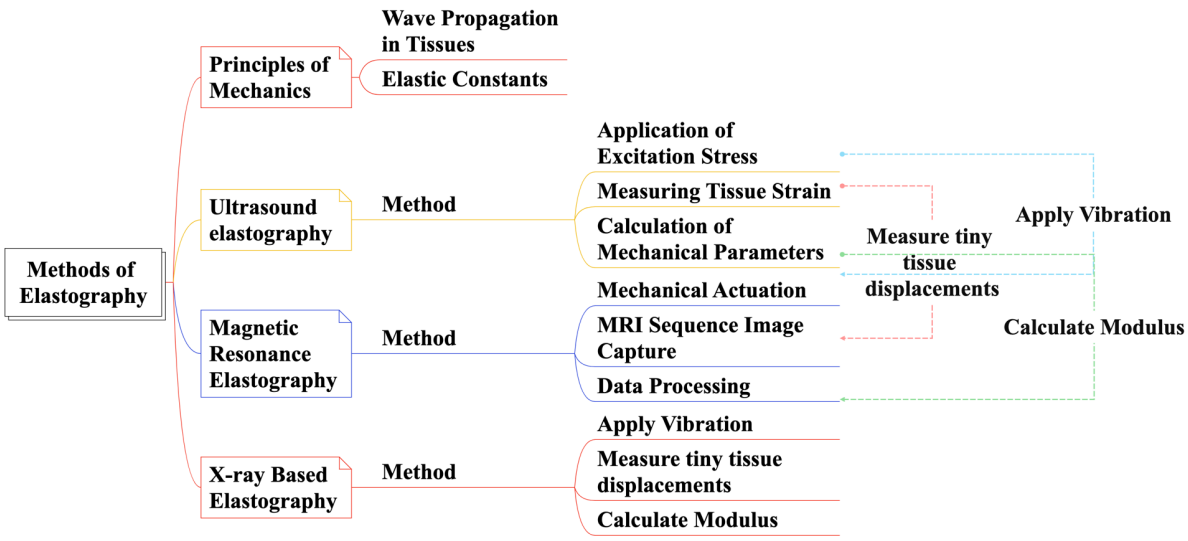

Figure 3. Methods of Elastography

2.2 Principles of Mechanics

2.2.1 Wave Propagation in Tissues

When a mechanical wave propagates through a medium like tissue, its behavior can be described by the wave equation. In a homogeneous isotropic medium, the wave equation is:

$$\nabla^2 u - \frac{1}{c^2}\frac{\partial^2 u}{\partial t^2} = 0 \tag{1}$$

where u is the displacement field, and c is the velocity of the wave.

The wave speed is related to the medium's elastic modulus (E) and its density (ρ) by:

$$c^2 = \frac{E}{\rho} \tag{2}$$

For tissues, which are often treated as incompressible, the elastic modulus relates more directly to the shear modulus, so we need to know the coefficient between this to constant [12].

2.2.2 Elastic Constants

Elastic modulus (E): In this situation, the elastic modulus is defined as the product of the square of the wave velocity and the density of the medium. The equation is:

$$E = \rho c^2 \tag{3}$$

where ρ is the density of the medium, c is the velocity of the wave [26]. It defines the rigidity of a substance. A higher modulus signifies a substance that resists deformation, implying it's rigid and hard. On the other hand, a diminished modulus points to a more flexible substance, soft.

Shear Modulus (G): also known as the relationship between elastic modulus and Poisson's ratio. The relationship is:

$$G = \frac{E}{2(1+\nu)} \tag{4}$$

where ν is the Poisson's ratio. It provides insight into a material's ability to resist shape changes when a force is applied parallel to one of its surfaces.

Bulk Modulus (K): Bulk modulus quantifies a material's resistance to uniform compression. It's expressed as the relationship with elastic modulus and Poisson's ratio. Mathematically:

$$K = \frac{E}{3(1-2\nu)} \tag{5}$$

where ν is the Poisson's Ratio. Substances with elevated bulk modulus, demonstrate resistance to volume alterations, rendering them largely impervious to compression under typical circumstances.

Most materials have Poisson's ratio values ranging between zero and 0.5. A material with a Poisson's ratio close to 0.5 tends to become much thinner when stretched, while one near zero tends to maintain its dimensions [13].

2.3 Ultrasound Elastography

Ultrasound elastography (UE) has evolved as a non-invasive tool offering valuable insight into the biomechanical characteristics of tissues, holding paramount importance in medical diagnostics, especially in detecting abnormalities such as tumors. The process of UE hinges on a simple premise: the elastic properties of tissues change when stress is applied.

When a material remains within its range of elasticity, any deformation it undergoes corresponds directly to the force exerted upon it, which causes shifts in widely recognized elastic attributes like the modulus of elasticity, volumetric modulus, rigidity modulus, and the coefficient of material compression. Besides these standard elastic coefficients, there are parameters associated with longitudinal and lateral aspects, which get deduced based on how quickly respective waves travel through solid substances. Ultrasonic elastography mainly

includes the following three steps: applying excitation stress, measuring tissue strain, and calculating mechanical parameters [3]. The following is a detailed discussion.

2.3.1 Application of Excitation Stress

In the domain of ultrasound-based elastography, tissues are subjected to stress either via mechanical pressure or through the force of acoustic radiation. A handheld probe is generally employed to give multiple, controlled compressions to the tissue's exterior. This permits exploration at diverse tissue depths by adjusting the compression's depth and range [14].

2.3.2 Measuring Tissue Strain

Following the stress application, tissues undergo deformation, and this deformation, known as strain, is what's primarily measured. Advanced imaging techniques, often employing radio frequency data, are used to gauge the tiny tissue displacements. The displacements can be on the order of micrometers, making precision and resolution critical factors for accurate measurements [15].

2.3.3 Calculation of Mechanical Parameters

Upon obtaining the strain metrics, they're subsequently turned into a visual layout or graphic that illustrates the variance in tissue rigidity. The proportion of imposed stress to observed strain illustrates the firmness or pliancy of the tissue. This derived elastography image visually portrays tissue firmness, allowing medical experts to distinguish between regular and possibly abnormal tissues by assessing their elastic characteristics.

2.3.4 Limitations of Ultrasound Elastography

Ultrasound Elastography has emerged as a promising diagnostic tool. However, like all medical imaging techniques, it is not without its limitations. The first one is operator dependency; the accuracy of the results can be significantly influenced by the technician's

proficiency. Differences in probe pressure or misalignment can lead to variances in measured elasticity [16]. The second is depth limitation. Ultrasound elastography is depth-dependent, meaning it can only analyze tissues and lesions located within a specific range from the skin surface. Deeper lesions or tissues might not be as effectively evaluated [15]. Third is Pre-compression Artifacts. Sometimes, the pre-compression applied by the transducer might deform the tissue before the actual measurements, possibly leading to misleading elastography data [17]. And the other one is limited resolution. Smaller lesions or those that are closely situated might be challenging to differentiate or even miss entirely due to the inherent resolution constraints of the technique [18]. And we cannot neglect the motion artifacts in regions close to major blood vessels or in organs like the lungs, the inherent motion can produce artifacts, compromising the reliability of elastography data [19].

2.4 Magnetic Resonance Elastography

Magnetic Resonance Elastography (MRE) is a non-invasive imaging modality that quantifies tissue stiffness by measuring the propagation of mechanically induced shear waves within the body using MRI. This technique allows for the visualization and estimation of tissue elasticity, offering insights into various pathological conditions [4]. The propagation speed of these shear waves is directly related to the tissue's stiffness: faster wave speeds indicate stiffer tissues, while slower speeds suggest softer tissues [7]. MRE mainly includes several steps: Mechanical Actuation, MRI Sequence Image Capture, and Data Processing. The following is a detailed discussion.

2.4.1 Mechanical Actuation

Mechanical actuation in MRE involves an external device producing low-frequency vibrations, typically ranging between 30 Hz to 60 Hz [20]. This actuator is placed on the body's

surface over the region of interest, which, when activated, generates harmonic waves that permeate the tissues. The intensity, frequency, and duration of these waves are critically important parameters, as they determine the depth of penetration and the tissue's response. The external actuation's safety and comfort are paramount; hence, advancements have been made in designing actuators to ensure minimal discomfort to patients while effectively generating shear waves within the tissues. Selecting the appropriate frequency is crucial since certain biological tissues resonate more effectively at specific frequencies, ensuring accurate and comprehensive imaging [21].

2.4.2 MRI Sequence Image Capture

Upon initiation of the mechanical actuation, a tailored MRI sequence, typically a phase-contrast sequence with modifications, is employed to capture the consequent tissue movements [22]. As the shear waves generated by the actuator propagate through the tissue, the MRI machine captures the minute displacements these waves induce. The choice of MRI sequence and parameters, such as repetition time, echo time, and slice thickness, are optimized for the specific region being imaged. Moreover, advancements in MRI technology have allowed for real-time imaging of wave propagation, enhancing the quality and accuracy of resultant elastography [23].

2.4.3 Data Processing

The collected wave data undergoes intricate processing using dedicated algorithms and inversion techniques to convert these wave images into elastography, which essentially depicts tissue stiffness [24]. Elastography provides color-coded maps with different colors or intensities representing different stiffness levels. The primary measure extracted is the speed at which the shear waves travel, with this speed being used to deduce the tissue's shear stiffness. This

inversion process is computationally demanding, and the quality of the resultant elastography heavily depends on the accuracy of the inversion algorithms. Current research is directed towards enhancing the resilience of these algorithms to various noise sources and improving their ability to handle complex tissue geometries and compositions [25].

2.4.4 Limitations of MRE

Despite its potential and numerous advantages, MRE has its limitations: While MRE can assess deeper tissues compared to ultrasound-based elastography, there's still a limitation on how deep the induced vibrations effectively penetrate [26]. The MRE procedure requires specialized equipment (like mechanical actuators) and post-processing software, demanding a long-time learning period and increased procedural time [27]. Patient movement during the MRE process can introduce artifacts, potentially confounding the results [28].

2.5 X-ray Elastography

In recent years, specifically, over the last ten years, X-ray elastography has surfaced as a potent tool in evaluating the mechanical attributes of tissues, overcoming several drawbacks of alternative imaging approaches. This methodology facilitates high-definition imaging while performing elasticity evaluations. X-ray elastography fuses the deep penetration capabilities of X-rays to gauge the rigidity of tissues, a critical indicator of pathological alterations. By amalgamating X-ray imaging tactics with mechanical oscillations or external influences, it becomes possible to visualize the elastic traits of tissues, providing a deeper understanding of their mechanical properties.

2.5.1 X-ray Elastography Evolution

Hamilton et al. elucidated a pivotal approach for X-ray elastography, where they emphasized the role of X-ray phase contrast images being modified by ultrasonic radiation

pressure. This intersection of X-ray imaging and ultrasonic radiation presented a novel method where the acoustic waves introduced slight deformations in the tissue. The modifications in the X-ray phase contrast images resulting from these deformations provided insights into tissue elasticity [5]. This interaction between ultrasonic radiation pressure and X-ray imaging presented a fundamental foundation for future research in the field.

2.5.2 X-ray Elastography Advanced Studies

Kim et al.'s seminal work took the concepts forward by computing strain images from 3D CT image data using a breast-mimicking phantom [29]. Their findings showcased the potential of extracting biomechanical properties from standard X-ray images. Kim and partners presented X-ray strain tensor imaging where they combined Finite Element Method (FEM) simulations with micro-CT experiments, achieving enhanced resolution and accuracy in strain measurements [30]. Chika Kamezawa and her partner used pneumatically vibrated polyacrylamide gel phantoms and obtained two-dimensional maps of storage and loss modulus, which were determined from temporal variation in displacement vectors of the vibrating particles in the phantoms. Their experiment provided storage modulus with a precision of 30%, and a spatial resolution was one order of magnitude higher than other imaging modalities [6]. One of the pivotal advancements in recent years was presented by Sutphin et al. They introduced elastography tomosynthesis using X-ray strain imaging of breast cancer. Their study effectively combined the high-resolution advantages of tomosynthesis, with elastography, enabling detailed strain evaluations in breast tissues. Their results provided compelling evidence for the adaptability of X-ray elastography in clinical settings, emphasizing its potential in early cancer detection and differentiation between benign and malignant lesions [31].

2.5.3 Future Research Directions

In the upcoming phase of my research study, I'm focusing on harnessing X-rays as the instrumental force to expose the selected specimen, coupled with the application of vibratory excitation. Using CT to generate two-dimensional images, when meticulously analyzed, has the potential to yield a comprehensive map detailing the elastic modulus of the specimen. This approach aims at achieving a detailed 2D CT-based elastography portrayal. With the integration of intricate computational mechanisms and traditional CT imaging, the goal is to transition into a three-dimensional arena, laying the foundation for CT-based dynamic elastography (CTDE). This advancement method would revolutionize how we detect the mechanical attributes of the materials or tissues under observation. I have summarized the research on elastography and identified subsequent research directions and details, as shown in Figure 4.

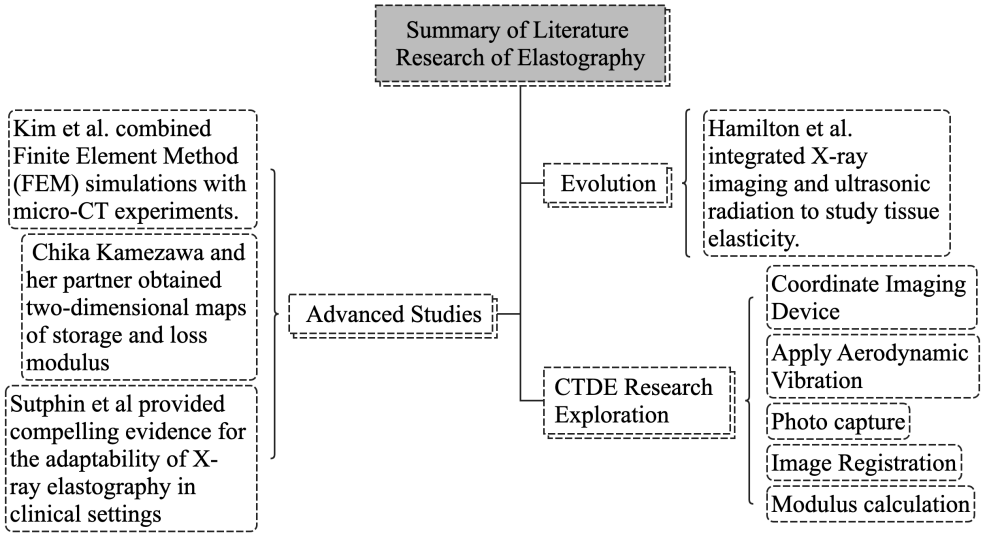

Figure 4. Summary of Literature Research of Elastography

Chapter 3. Methodology of Achieving CT-based Dynamic Elastography

In the realm of scientific inquiry, meticulous investigation often paves the way for significant breakthroughs. Following an exhaustive exploration into the intricacies of elastography, I have summarized a set of pivotal steps imperative to achieving meaningful outcomes in this domain. This chapter endeavors to delve into these steps in-depth and develop a simulation methodology for CTDE. Such basic work is crucial not merely for theoretical understanding, but to also ensure that subsequent simulation validations are robustly equipped and executed, as shown in Figure 5.

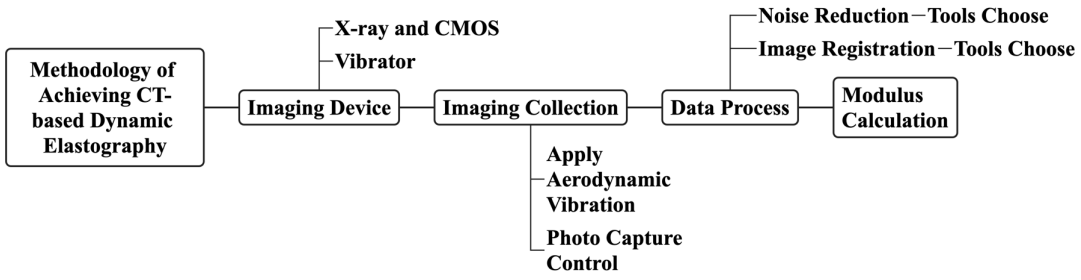

Figure 5. Methodology of Achieving CT-based Dynamic Elastography

3.1 Imaging Device

A central element in the apparatus of X-ray elastography is the X-ray detector. The sensitivity and resolution inherent in the detector play a vital role in delineating the detailed deformation under the applied shear wave propagation. State-of-the-art detectors facilitate enhanced spatial resolution, paving the way for more precise analyses of the permeable X-ray, which provides more detailed views into the elastic properties of tissues.

3.1.1 X-ray and CMOS

Within the frontier of progressive research, the instruments and tech solutions we leverage have a substantial bearing on the results of our research and scholarly undertakings. In the context of our experiment, while both the emitter and receiver of X-rays are undeniably crucial, I posit that the receiver holds paramount importance. Our primary objective is to document tissue deformations post mechanical wave stimulation. Therefore, it stands to reason that heightened attention and effort should be directed towards the receiving end. An important instrument that I am eager to incorporate into my impending research is the X-ray camera fortified with the sCMOS 16MP Detector. Its appeal is straightforward: it offers a peerless amalgamation of swift capturing velocity coupled with outstanding resolution. The shortest capture span of this apparatus clocks in at 50 microseconds, a duration amply satisfying the needs for photography at the millisecond scale following the initiation of mechanical vibrations. The combination of fast acquisition speed and best-in-class resolution makes the X-ray camera with sCMOS 16MP detector the ideal device for my real-life experiments [32]. The instrument's combination of speed and accuracy promises a surge in the quality of data acquired, thereby improving comprehensive research outcomes. But I didn’t use it in my simulation, I use the FEM instead.

3.1.2 Vibrator

In future research, I intend to use pneumatic vibration to impose mechanical waves onto the test subjects. Pneumatic vibration, in the realm of experimental mechanics and biomedical research, has increasingly become a foundational technique for imposing mechanical waves onto test subjects. Essentially, a pneumatic vibration table generates mechanical vibrations, which are then transmitted through air to the object being tested. This approach ensures a contact-free delivery of mechanical perturbations, eliminating potential biases from direct mechanical

interfaces. A standout application of pneumatic vibration lies in its extensive use in the clinical context of Magnetic Resonance Elastography [4].

Opting for pneumatic vibration provides several benefits. First, by decoupling the vibration source from the test subject, there's a significant reduction in the risk of transmission of unintended mechanical disturbances, leading to cleaner, more precise readings, as shown in Figure 6. Second, this method enables the customization of vibration frequencies and amplitudes, offering flexibility in experimental setups tailored to specific clinical scenarios.

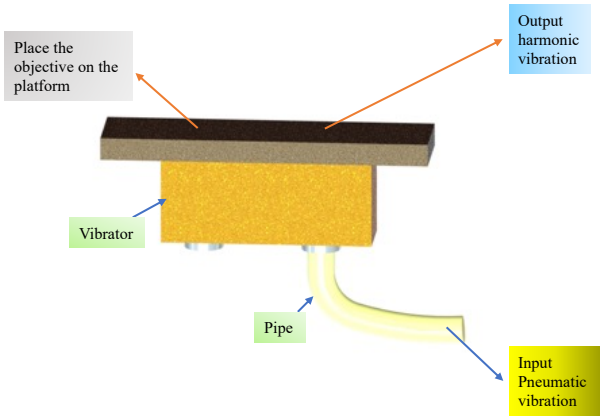

Figure 6. Diagram of Pneumatic Vibrator

In conclusion, the pneumatic vibration method stands out not just for its technological sophistication but also for its practical utility. By ensuring that mechanical waves are delivered in a consistent, controlled, and non-invasive manner, this technique solidifies its role as an indispensable tool, particularly in MRE clinical settings. Its blend of reliability and precision promises to continually shape and advance future research endeavors.

3.2 Imaging Collection

3.2.1 Apply Aerodynamic Vibration

In the practice of elastography imaging, the initiation of aerodynamic vibration to the focal specimen stands as a critical procedure. This involves unleashing a fixed shear wave to provoke microscopic alterations in the entity under scrutiny. These alterations, albeit tiny, hold significant value in deducing the suppleness and mechanical attributes of the tissue or material in examination. It is imperative to recognize that inherent disparities exist in natural structures, particularly in biological tissues, featuring diverse cellular elements and extracellular environments.

Therefore, the advent of shear waves triggers a range of deformation magnitudes in different zones of these tissues, a phenomenon spurred by disparities in aspects like density, elasticity, and overall tissue constitution. Hence, during an elastography assessment, the deformation patterns witnessed are a rich source of critical data. The differences in deformation scale across various areas are authentic indicators, mirroring the fundamental structural and mechanical distinctions present. Utilizing these divergent reactions, elastography furnishes a detailed representation of the specimen's physical properties, thus facilitating a more enlightened comprehension of its shape and possible pathological conditions.

3.2.2 Photo Capture Control

Prior to initiating the vibrational procedure, it is essential to capture a baseline image of the specimen. This preliminary image serves as a reference point, facilitating the identification of changes or deformations induced by the subsequent vibrations. Once the vibration is applied, an additional set of four images is systematically taken over the course of the vibrational period.

The rationale for capturing these images during the vibrational phase lies in the nature of the applied wave, which exhibits a simple harmonic motion.

Given this harmonic nature, each of the four images should ideally represent the specimen's state at every quarter of the wave's period. Such a strategic capturing sequence ensures that the full spectrum of the wave-induced deformation is documented comprehensively, spanning from the point of initial disturbance to its maximum displacement and back to its point of rest, as shown in Figure 7. However, this meticulous imaging strategy necessitates highly sophisticated equipment. The camera's shutter speed must be fast, with transient motions induced by the vibrations, capturing clear, undistorted images. Furthermore, the precision of the controlling mechanism is of paramount importance. Any inconsistency or time lag, no matter how minute, can jeopardize the accuracy of the results. Therefore, to ensure the reliability and validity of the elastography data, coordinate control of these devices is indispensable.

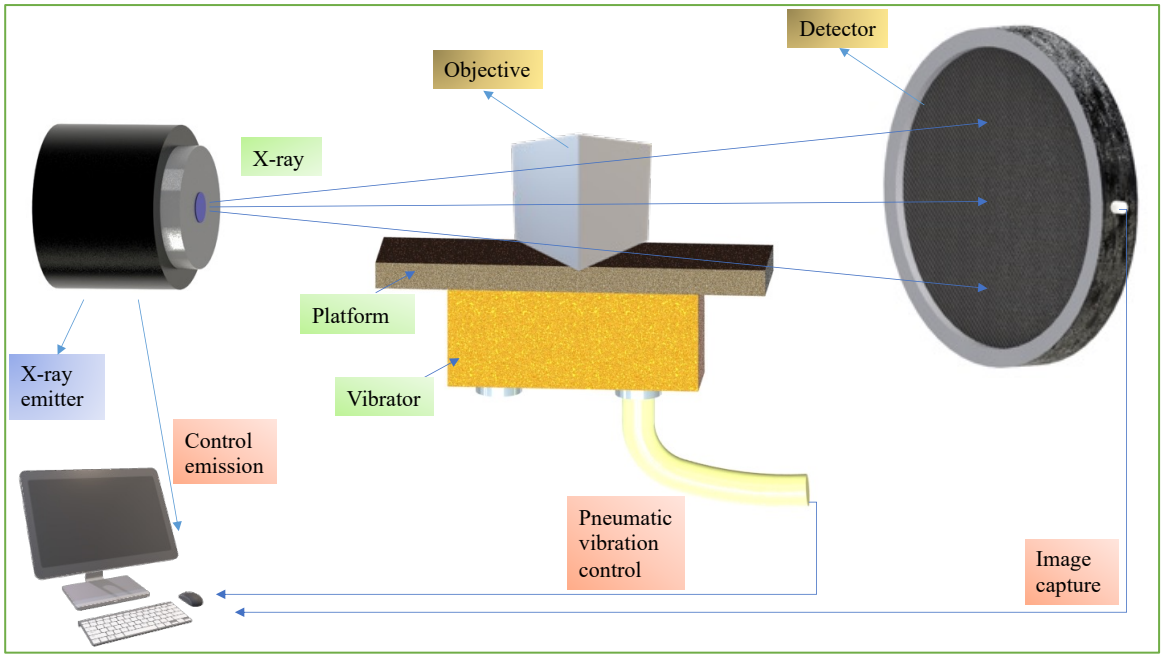

Figure 7. Diagram of the Experiment

3.3 Data Process

In the tapestry of our experimental design, data processing emerges as one of its most vital threads. The raw image data we acquire undergoes meticulous layer-by-layer refinement, allowing us to extract the precise datasets intended for our computational design. The processes of denoising and registration stand out as the linchpins of our data-handling approach. Having gathered and familiarized myself with a selection of the most apt methodologies for both denoising and registration, I am poised to delve deeper into their nuances in the ensuing discussion, as shown in Figure 8.

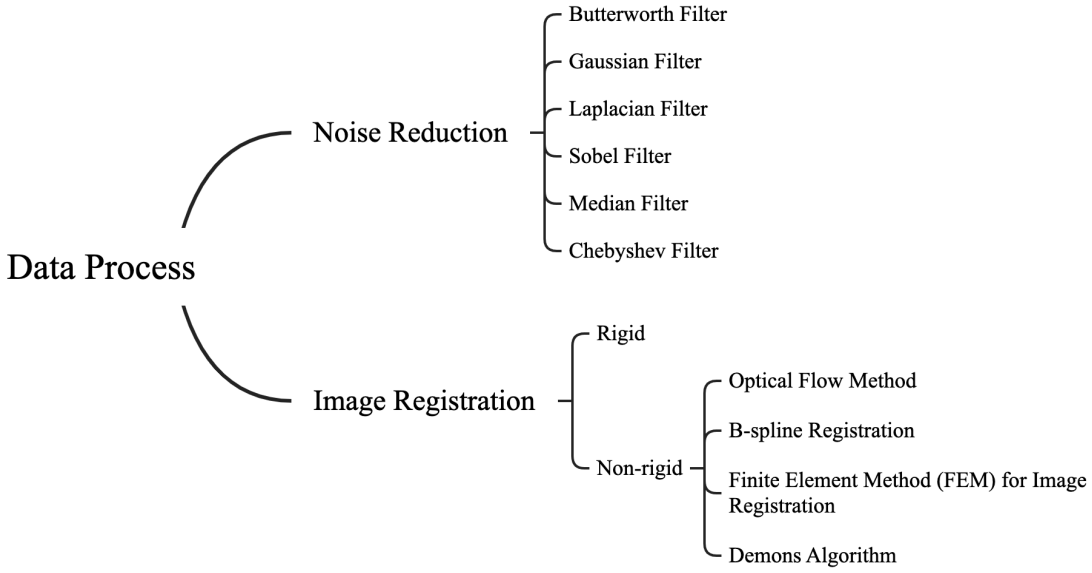

Figure 8. Data Process Methods and Systems

3.3.1 Noise reduction

Ensuring the highest possible quality of the captured picture in elastography studies is of paramount significance. One of the primary challenges in achieving this is mitigating the noise

present in the picture data. The intrusion of noise into the picture not only hampers the clarity of visual information but also critically undermines the precision of the extracted data. It can introduce discrepancies that, if we cannot reduce them, may distort the findings, leading to errors.

When these noisy pictures are subjected to image registration, a process that aligns and overlays multiple images to derive coherent data, the negative impact of noise becomes even more pronounced. The registration process relies heavily on the consistency and integrity of pixel values between sequential frames. Noise disrupts this consistency, posing challenges in achieving non-rigid registration and causing potential misalignments. These misalignments, however minute, can accumulate over sequences and diminish the reliability of the entire dataset.

Therefore, adopting an effective noise reduction technique isn't just a choice; it's a necessity. By filtering out extraneous noise while preserving the vital details of the image, the chosen noise reduction method can enhance the fidelity of the video. This, in turn, ensures that subsequent analytical processes, like image registration, are performed on clean, accurate data, significantly boosting the credibility of the results. In summary, a judicious selection of a noise reduction method is a foundational step that sets the stage for the success of the entire research study.

3.3.1.1 Butterworth Filter

The Butterworth filter, often referred to as the "maximally flat magnitude filter," occupies a unique position in the domain of signal processing. Its conception can be traced back to the innovative work of the British engineer Stephen Butterworth. In his seminal paper, "On the Theory of Filter Amplifiers" published in 1930 [33], Butterworth introduced a filter design that would subsequently be ingrained in a multitude of applications, owing to its attributes.

The filter’s order determines the transition's sharpness from the passband to the stopband. As the order increases, the roll-off becomes steeper, providing clearer delineation between maintained and attenuated frequencies [34]. However, this clarity often comes at the cost of design complexity and potential realization challenges, especially when real-time processing is in the picture.

Despite its commendable flat passband, it isn't without limitations. A notable limitation is its relatively gradual roll-off in comparison to alternative filter designs like the Chebyshev or elliptic filters [35]. This implies that, given the same order, a Butterworth filter might inadvertently allow more unwanted signals in the transition zone between its passband and stopband, as shown in Figure 9. Still, in contexts where a ripple-less, gentle transition outweighs the need for a sharp cutoff, it emerges as the preferred choice. It finds its place in diverse applications, ranging from audio engineering and telecommunications to the intricate realm of biomedical signal processing [36].

(a) (b)

Figure 9. (a) is the origin, and (b) has undergone a Butterworth filter.

To sum it up, the Butterworth filter, renowned for its maximally flat frequency response and straightforward design parameters, continues to be a mainstay in signal processing applications. While not a panacea for all situations, its consistent and predictable behavior cements its status as a valuable tool in the signal processing library.

3.3.1.2 Gaussian Filter

The Gaussian filter, often recognized as the Gaussian smoothing operator, finds a wide range of applications in the realms of image processing, computer vision, and signal processing. This filter is characterized by its bell-shaped curve, which is defined by the Gaussian function. The central idea behind this filter is the concept of convolution, where an original signal or image is combined with the Gaussian function to produce a smoothed version [37].

Mathematically, it is defined by the Gaussian function:

$$G(x) = \frac{1}{\sqrt{2\pi\sigma^2}} \exp\left(\frac{-x^2}{2\sigma^2}\right) \tag{6}$$

where, σ denotes the standard deviation, determining the width of the bell curve. This function showcases how values farther from the center fall off exponentially, thus ensuring that only pixels or data points in the immediate vicinity have a prominent influence when filtering [38].

In image processing, it is extensively used for blurring and noise reduction. Images often come with a certain amount of noise, either due to sensor anomalies or transmission errors. Gaussian smoothing aids in attenuating high-frequency noise, making the underlying image features more prominent. This kind of blurring is not just indiscriminate smudging but is grounded in the spatial distribution defined by the Gaussian function. As a result, it gives more weight to the nearby pixels and less to the distant ones in a non-linear fashion, as shown in Figure 10 [39].

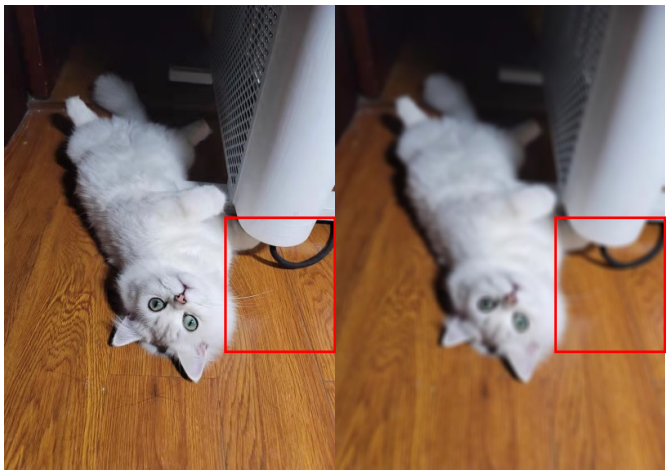

(a) (b)

Figure 10. (a) is the origin, and (b) has undergone a Gaussian filter.

It has also found its way into edge detection algorithms. When combined with other operators, such as the Sobel operator, it can assist in identifying sharp intensity variations in images, which correspond to edges [40]. The beauty of the Gaussian filter lies in its adaptability to multi-dimensional data. While the function mentioned earlier represents a 1-dimensional Gaussian, it can be expanded to 2D, 3D, and beyond. For instance, in 2D, the equation became:

$$G(x,y) = \frac{1}{\sqrt{2\pi\sigma^2}} \exp\left(-\frac{x^2+y^2}{2\sigma^2}\right) \tag{7}$$

This 2D version is particularly valuable in image processing, where both x and y spatial coordinates are considered [41].

To sum up, the Gaussian filter remains an integral component in various signal and image processing tasks due to its versatile applications. Its foundation in the Gaussian function ensures a natural and effective weighting scheme, leading to smoothed outputs that retain essential features while discarding noise.

3.3.1.3 Laplacian Filter

The Laplacian Filter is one of the foundational tools used in the domain of image processing for the purpose of edge detection and image sharpening. Fundamentally, it is a second-order derivative mask that can highlight regions of rapid intensity change in an image and is particularly sensitive to noise [37].

The Laplacian is mathematically represented by the divergence of the gradient of an image function. In two-dimensional space, provides a measure of the second derivative in the x and y directions. When applied to an image, it essentially computes the difference between a pixel's value and the average of its surrounding pixels. This difference often leads to the detection of edges within the image where there's a rapid transition of intensity [38], as shown in Figure 11.

Figure 11. (a) is the origin, and (b) has undergone a Laplacian filter.

It is especially useful for detecting edges in images. However, one must note that it might detect edges that are not perceptually significant. The zero-crossings (where the value of the filter changes sign) typically represent the locations of edges in the image [40]. The output of it can be subtracted from the original image to produce a sharpened version of the image. This

technique enhances the edges, making the image appear clearly [42]. A notable characteristic of the Laplacian filter is its sensitivity to noise. Since it's a second-order derivative, even minor variations in intensity can get amplified. As a result, it's common to first apply a smoothing filter (like a Gaussian filter) before applying the Laplacian for edge detection [43].

In conclusion, while it is a powerful tool in image processing, particularly for edge detection and image sharpening, careful preprocessing and postprocessing steps are crucial to ensure optimal and noise-free results.

3.3.1.4 Sobel Filter

The field of image processing has numerous tools to aid in edge detection, one of the most widely used among them being the Sobel filter (or Sobel operator). Fundamentally designed for edge detection, it emphasizes the boundaries where intensity variations are most noticeable in an image [37]. It works by calculating the gradient magnitude of an image intensity function. At every pixel in the image, the gradient points in the direction of the largest possible intensity increase and has a magnitude equal to the rate of change in that direction. With this, it's possible to get a fairly accurate measurement of the directional change in intensity, highlighting the edges [44].

It utilizes two 3x3 convolutional kernels, one estimating the gradient in the x-direction (horizontal) and the other estimating the gradient in the y-direction (vertical). These kernels are designed to respond maximally to edges running vertically and horizontally relative to the pixel grid, providing a measure of intensity change in respective directions [38].

When these masks are convolved over an image, they produce what's known as the gradient components for each direction. The magnitude and direction of the gradient can then be computed from these components [45].

The primary application of the Sobel operator is edge detection. Its ability to provide a clear delineation of intensity changes makes it a cornerstone in many edge-based image processing tasks [40]. By highlighting the edges, it can be used to enhance the overall clarity and definition of images, making details more distinguishable, as shown in Figure 12.

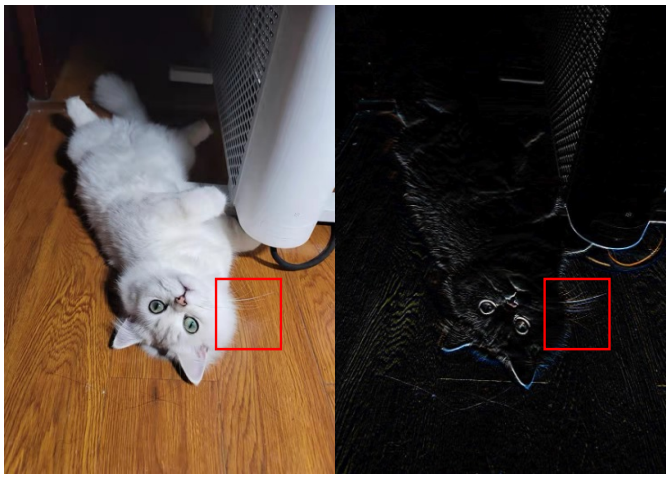

Figure 12. (a) is the origin, and (b) has undergone a Sobel filter.

It is sensitive to noise. It's often beneficial to preprocess an image using a smoothing filter before applying the Sobel operator to reduce the risk of amplifying the noise [42]. The direction of the gradient can provide information about the orientation of the edge. By computing the arctangent of the ratio of the two gradient components, one can infer the direction of the edge at every pixel [47]. By combining the gradient components from both directions, the magnitude or strength of the edge can be computed. This is often done using the Pythagorean theorem, providing a single value representing the strength of the edge [43].

While it is robust in detecting edges, it does have its limitations. Its linear and relatively small-sized kernels make it less effective in detecting more subtle or curved edges. Also, as with

most edge detectors, it is sensitive to noise and may require preprocessing for optimal results [48].

3.3.1.5 Median Filter

Image noise is an inevitable issue in digital imaging, which can degrade image quality and impact subsequent analysis. One of the traditional and widely used techniques to address noise, in digital images is the Median Filter [37]. It operates in a straightforward manner by moving through the image pixel by pixel, replacing each value with the median value of neighboring pixels. This neighborhood is typically a square but can be any shape, and its size is generally defined by the user depending on the specific application [46]. For a grayscale image, if we consider a 3x3 neighborhood, it contains 9-pixel values. These values are sorted, and the middle value is selected. The central pixel of the 3x3 neighborhood is then replaced by this median value.

One of the most notable advantages of the Median Filter is its ability to retain edge information while removing noise. This is particularly beneficial in scenarios where the preservation of edges is crucial, such as in medical imaging or object detection applications [38]. In comparison to mean or linear filters, which blur the image and might lead to edge loss, it has shown superior performance in preserving useful information.

It has found its applications across a wide range of fields. It's extensively utilized in digital image processing, especially in preprocessing steps. For example, in computer vision applications, before extracting features or detecting objects, the image is often passed through a median filter to ensure noise reduction without compromising on the sharpness of the image [45]. In medical imaging, where the clarity of images can directly impact diagnosis and patient care, median filters play an essential role in enhancing image quality by suppressing noise while

retaining the details of organs, tissues, and other structures [49]. While it is potent against certain types of noise, it may not be the best choice for all noise types or applications. Furthermore, although it preserves edges, it might smooth out fine image details if applied aggressively or repeatedly, as shown in Figure 13. Therefore, a balance between noise reduction and detail preservation should be carefully considered [48].

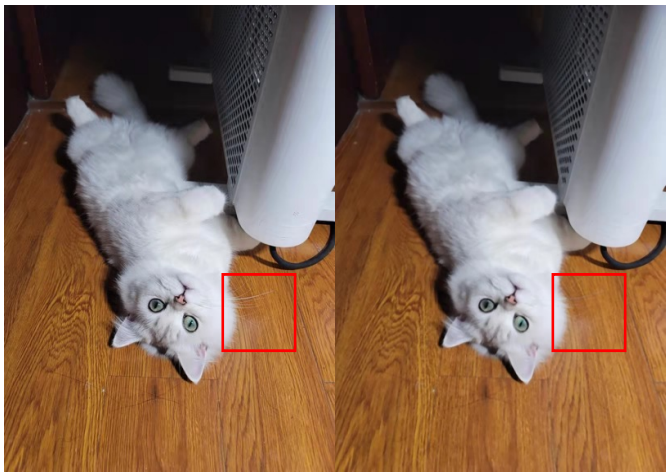

(a) (b)

Figure 13. (a) is the origin, and (b) has undergone a Median filter.

3.3.1.6 Chebyshev Filter

Filters are critical components in signal processing, aiding in the isolation of desired signals from undesirable noise or interference. The Chebyshev Filter, a particular type of filter design, stands out due to its unique characteristics in the frequency response caused by its equal ripple behavior, as shown in Figure 14 [34]. It is categorized based on their ripple behavior in the passband. There are Type I and Type II Chebyshev filters, with Type I exhibiting an equal ripple behavior in the passband and a monotonic behavior in the stopband, whereas Type II showcases the opposite behavior [50].

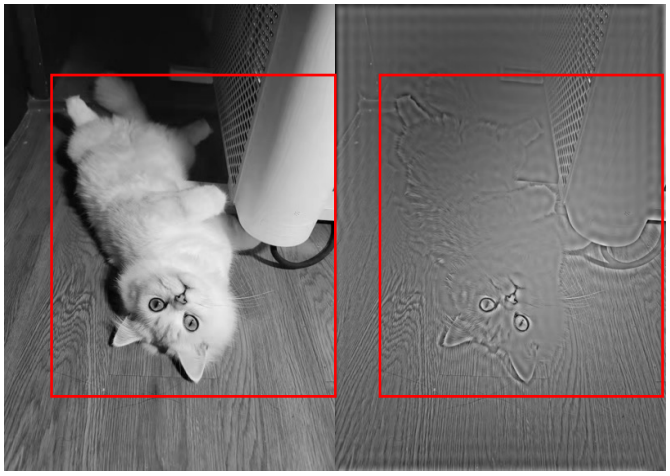

(a) (b)

Figure 14. (a) is the origin, and (b) has undergone a Chebyshev filter.

The primary advantage of it is its steeper roll-off characteristics compared to the Butterworth filter. This means that Chebyshev filters can transition from the passband to the stopband more rapidly, making them desirable in applications that require strict band separation [51]. Chebyshev filters are employed in various fields, especially where a rapid transition between frequency bands is essential. Their applications span audio processing, radio frequency design, and even biomedical signal processing. For instance, in radio receivers, where isolating a particular channel or frequency is critical, the sharp roll-off of Chebyshev filters is highly beneficial [35]. It offers a unique balance between roll-off sharpness and ripple magnitude. Its design flexibility, derived from the Chebyshev polynomials, makes it a popular choice for many signal processing applications.

3.3.2 Image Registration

Medical image registration is a critical component in the field of medical imaging, aiding in the alignment of two or more images of the same region captured at different times, from different angles, or even by different modalities. This alignment process has been integral to

enhancing the analysis and interpretation of medical images, thereby assisting medical professionals in diagnosis, treatment planning, and monitoring the progression of diseases. At its core, the primary objective of image registration is to determine a transformation that will best align features in the images under consideration.

3.3.2.1 Fundamental Principles

At the heart of medical image registration lies the core tenet of spatial alignment, which is to overlay two or more medical images such that the anatomical structures within them are correspondingly positioned. These images could be taken from the same modality at different instances or derived from entirely different imaging modalities. Achieving precise alignment is no simple task, given the potential for anatomical variations and differences in patient positioning across scans. Furthermore, discrepancies in imaging techniques, inherent noise, or resolutions can compound the challenge. The objective then becomes the determination of a spatial transformation, which, when applied, makes these images congruent or brings them to a common spatial framework. This transformation program is iteratively adjusted to optimize certain criteria or metrics, effectively minimizing the variance between the reference and the target image. The success of the registration process hinges on the accuracy of this transformation, which then ensures that the overlapping structures between the images are anatomically consistent.

3.3.2.2 Registration Approaches

Medical image registration can be broadly classified based on the nature of transformations into two categories: rigid and non-rigid.

Rigid registration primarily involves transformations like rotation and translation that don't modify the image's shape or size. This type of registration is apt for anatomical structures that

remain largely unchanged across different images. For example, the skull, being a rigid structure, doesn't deform over time, making rigid registration ideal for brain imaging.

In contrast, non-rigid registration accounts for deformable transformations, allowing images to be bent, stretched, or compressed to achieve alignment. Given that the human body is replete with soft tissues that can change shape and position, owing to breathing, muscle contractions, or even pathological conditions, non-rigid registration becomes indispensable.

These approaches are not mutually exclusive and can be combined in hierarchical methods where rigid registration serves as an initial alignment step, followed by fine-tuning through non-rigid methods. Next, we discuss the image registration method in detail.

3.3.2.3 Optical Flow Method

Optical flow is a fundamental concept in the domain of computer vision and image processing that pertains to the apparent motion of brightness patterns in a visual scene. It offers a means to infer the pattern and speed of objects' movement across a sequence of frames, most typically in a video. The inherent basis for optical flow is the temporal variation of image intensity. It operates under the assumption that the intensity of a pixel remains consistent over short periods of time, even as it moves from one position to another.

Optical flow can be described as the distribution of the apparent velocities of movement of brightness patterns in an image. It's important to understand that optical flow doesn't measure actual object velocities but rather captures the temporal change in intensity patterns. The fundamental constraint here is the brightness constancy constraint, which assumes that a particular pixel's brightness (or intensity) does not change between consecutive frames, though its position might [52].

Typically, optical flow algorithms aim to minimize the error in the brightness constancy constraint. Among the first and most influential techniques for optical flow computation is the Lucas-Kanade method, which employs a local approach using image gradients to compute the flow parameters [53]. Conversely, the Horn and Schunck method takes a global approach, factoring in the smoothness of the entire flow field. Over the years, numerous other methods, such as the Farnebäck algorithm and the Brox method, have been developed, each with its strengths and drawbacks [54].

Optical flow finds a broad spectrum of applications. In video compression, it aids in predicting frame sequences, thereby saving data. Robotics and autonomous vehicles, support navigation by analyzing scene dynamics. It's invaluable in understanding and interpreting human activities in surveillance videos. Furthermore, in computer graphics, optical flow assists in tasks such as video stabilization, video synthesis, and even in generating slow-motion sequences from standard footage [55].

Despite its potential, optical flow is not without its challenges. It is often sensitive to noise in images, and luminance changes can lead to incorrect flow estimations. The aperture problem, inherent to optical flow methods, defines the challenge of determining the correct motion direction of an edge when only the velocity perpendicular to the direction of the edge's gradient is known. Additionally, methods like Lucas-Kanade can struggle with large displacements due to their local nature [45].

The advent of deep learning has significantly impacted the optical flow domain. Deep learning-based methods, such as Flow Net, PWC-Net, and Lite Flow Net, have set new benchmarks in optical flow estimation, exhibiting remarkable accuracy improvements over traditional methods. These neural network models are trained on vast datasets and can capture

complex motion patterns, even in challenging scenarios. Furthermore, the integration of optical flow with other sensors, like depth cameras, is paving the way for more robust motion analysis, especially in 3D space [56].

Optical flow, with its ability to capture and represent motion in visual scenes, remains a cornerstone in the realm of computer vision. While traditional methods laid the foundation, the integration of modern machine learning techniques is pushing the boundaries of what's achievable. As technology continues to evolve, the precision and application range of optical flow methods are set to expand exponentially.

3.3.2.4 B-spline Registration

B-spline registration is a flexible and popular technique used predominantly in the field of medical image processing to map anatomical structures from one image to another. Its adaptability, precision, and ability to model complex deformations have made it a go-to method for many researchers and professionals.

B-splines, or Basis splines, were introduced in the 1970s and have since been extensively used in computer graphics and geometric modeling. They represent a piecewise-defined polynomial function that can effectively model complex, free-form shapes with a high degree of smoothness [57].

In the context of image registration, B-splines can be used to denote a transformation field. A grid of control points is defined over an image. The transformation of every image voxel is computed as a weighted sum of the surrounding control point transformations. The degree of influence a control point has over a voxel is determined by the B-spline basis function. Higher-degree B-splines allow smoother and more gradual transformations, whereas lower-degree B-splines are more localized [58].

B-spline registration can model both global and local deformations, providing a broad range of transformations, from rigid and affine to highly non-rigid [59]. The inherent smoothness of the B-spline functions ensures that the resulting transformation is continuous and differentiable, which is especially critical in medical imaging applications where the physical plausibility of deformations is vital as shown in Figure 15 [60]. Due to their piecewise nature, B-splines are computationally efficient, especially when combined with multi-resolution strategies [58].

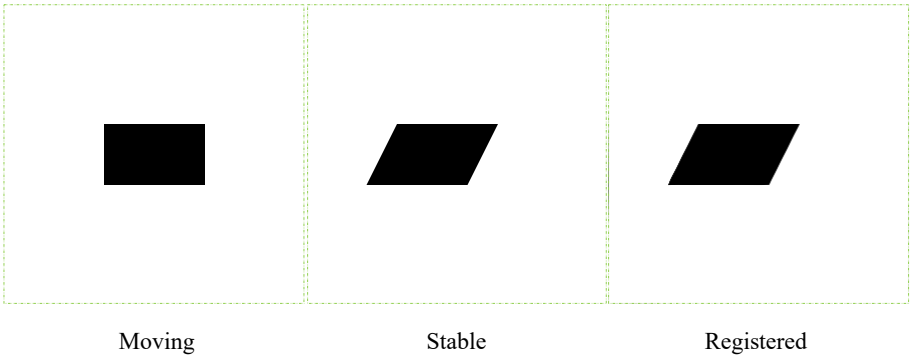

Figure 15. The "Registered" image is obtained by registering the "Moving" image to the "Stable" image using the b-splines method.

B-spline registration is predominantly used in medical imaging, including applications like inter-patient image registration, where one patient's images are aligned with another's; intra-patient registration, where images of the same patient from different times or modalities are aligned; and atlas-based segmentation, where a known atlas is deformed to fit a new image for segmentation purposes [61].

Despite its advantages, B-spline registration does have limitations. The quality of registration depends largely on the chosen grid spacing of control points. Too coarse a grid may miss localized deformations, while too fine a grid may become computationally expensive and overfit noise.

In conclusion, B-spline registration has proven to be an indispensable tool in the world of image processing, particularly in medical applications. Its ability to seamlessly integrate global and local deformations with computational efficiency has made it a popular choice among professionals and researchers alike.

3.3.2.5 Finite Element Method for Image Registration

Image registration is a critical task in image processing, often employed to align two or more images of the same scene taken at different times, from different viewpoints, or by different sensors. Over the years, numerous methods have been developed to address the complex challenges inherent in image registration, and among them, the FEM stands out as a particularly potent tool, especially for non-rigid registration tasks.

The FEM, historically rooted in engineering and physical sciences for solving boundary value problems, has found its way into the realm of medical imaging and image registration [62]. FEM decomposes the image domain into a mesh of smaller, finite elements, like triangles or tetrahedra. The deformation or transformation is then computed within each of these small elements, allowing for a high degree of flexibility and precision.

At its core, FEM aims to find an approximate solution to a boundary value problem by discretizing the problem's domain. In the case of image registration, this entails determining a deformation field that maps one image onto another. The deformation field is represented using a set of basic functions defined over the finite elements, and the registration problem boils down to optimizing the coefficients of these basis functions [63].

The primary advantage of FEM is its inherent ability to model complex deformations with high precision. Due to its roots in physical modeling, FEM can incorporate biomechanical properties, making it especially suited for registering images of anatomical structures that

undergo non-linear and non-uniform deformations, like the human brain or the heart [64]. The method's flexibility also allows it to be adapted to various image modalities and registration scenarios.

Given its ability to model complex deformations, FEM has been extensively used in the medical imaging domain. For instance, in neuroimaging, FEM-based approaches have been employed to register MRI scans of the brain, considering the brain's biomechanical properties [65]. Similarly, in cardiology, FEM has been used to register images of the heart taken at different stages of the cardiac cycle.

The field of image registration is dynamic, with constant innovations and improvements. There's a growing interest in integrating machine learning techniques with traditional methods like FEM to enhance registration performance [66]. Additionally, as computational power increases, the feasibility of employing even more detailed and high-resolution finite element models in real-time registration scenarios becomes a tangible reality.

While FEM offers significant advantages, it is computationally more demanding than some other registration methods, especially when high-resolution meshes are used [67]. Also, the accuracy of FEM-based registration can be influenced by the quality of the mesh. Poorly defined or overly coarse meshes might not capture fine deformations. Another challenge is defining appropriate boundary conditions and material properties when employing FEM in a biomechanical context.

In summary, the FEM offers a robust and flexible approach to tackle the challenges of non-rigid image registration. Its foundation in physical modeling, combined with its mathematical rigor, makes it a vital tool in the library of image processing techniques, especially in applications demanding high precision and biomechanical fidelity.

3.3.2.6 Demons Algorithm

In my research, I use the Demons algorithm to make image registration [68]. At its core, the Demons algorithm operates on the principle of optical flow. It seeks to estimate the apparent motion of brightness patterns in the image. The basic assumption guiding the algorithm is that the intensity of an image structure remains unchanged as it moves from one spatial position to another. In the context of medical images, this assumption translates to the idea that the intensity of a particular anatomical structure remains consistent across different images, even if its spatial position varies.

Under the Demons framework, the displacement field, which denotes the transformation required to align the moving image to the fixed one, is iteratively updated. This is achieved by estimating local "forces" based on the difference in image intensities and gradients. The forces act as vectors, guiding the transformation required at each pixel or voxel to improve alignment. Here is an example that use demons' method to register the moving picture to the stable picture, as shown in Figure 16.

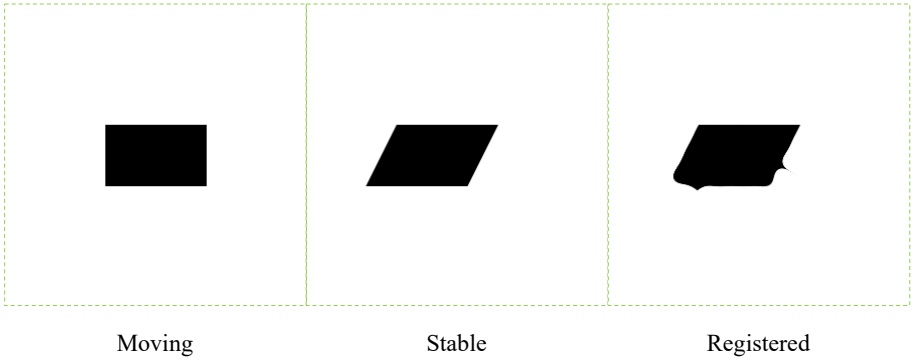

Figure 16. The "Registered" image is obtained by registering the "Moving" image to the "Stable" image using the Demons Algorithm.

The Demons algorithm's primary strength lies in its simplicity and efficiency. Because it relies on intensity information and does not necessitate the extraction of complex features or landmarks, it can be applied to a wide range of images. Furthermore, the algorithm is particularly adept at handling local deformations, making it well-suited for non-rigid registration tasks.

Its applications span various medical imaging domains, including but not limited to neuroimaging, lung imaging, and oncological imaging. In these areas, the Demons algorithm assists in temporal studies (tracking anatomical changes over time) and multi-modal image fusion, where images from different modalities, like MRI and CT, need to be aligned.

3.4 Modulus Calculation

Understanding the mechanical properties of materials, especially their modulus, is crucial in numerous applications spanning from engineering to biomedical fields. One innovative approach to determining the modulus of a material is by leveraging displacement maps. A displacement map, in essence, provides a spatial distribution of displacements in a material when subjected to external forces or deformations. Through analyzing this displacement pattern, we can infer key mechanical properties, primarily the modulus, which defines the material's resistance to elastic deformation.

A displacement chart, frequently created through imaging methodologies or computational analyses, records the comparative movements of distinct areas within a substance under the effects of stress or strain. It graphically illustrates the movements or deformations occurring in different sectors of the material. The fineness and correctness of this chart hold paramount importance as they influence the exactitude of ensuing modulus evaluations directly.

Upon securing a displacement chart, the inaugural move is determining the strain the material undergoes. Strain signifies the deformation degree, illustrating the shifting occurring between particles in the material's composition. This can be inferred from the displacement chart by scrutinizing the relative shifts occurring between divergent sectors.

In my study, the external stimulation employed is the shear wave. Because of utilizing this specific type of wave, it becomes imperative to calculate the shear modulus. The shear modulus, often denoted as the modulus of rigidity, represents the material's ability to deform elastically under shear stress without experiencing any change in volume. It provides key insights into the mechanical properties of the material in question, especially in response to shear forces.

To determine the shear modulus, a fundamental preliminary step involves calculating the propagation speed of the mechanical wave within an elastic medium. The speed at which this wave traverses the material is contingent upon the medium's intrinsic properties and is directly linked to its rigidity and density. A faster propagation speed typically denotes a stiffer (or more rigid) material.

Given the significance and intricacies of this calculation, we adopted the phase gradient method for assessing wave speed. This method offers advantages in terms of accuracy and precision. The phase gradient technique harnesses the spatial derivatives of the captured wave phase to provide a robust estimation of the wave's speed. By integrating these accurate wave speed measurements with the known relations governing wave propagation in elastic media, we can derive a precise value for the shear modulus, enhancing the reliability and applicability of our findings. Mathematically:

$$\mathrm{C} = 2\pi f \frac{\Delta u}{\Delta \varphi} \tag{8}$$

where C is the velocity of the shear wave, f is the excitation frequency, Δu is the distance change, $\Delta\varphi$ is the phase change [26].

Chapter 4. 2D CT-based Dynamic Elastography Simulation

4.1 Simulation Method

Following our preliminary investigations, I've deduced that to accomplish CT-based dynamic elastography. First, we need to obtain deformation maps of the test object post-aerodynamic vibration. This procedure can be effectively conducted within the confines of COMSOL Multiphysics. This software is tailored for simulating real-world Multiphysics phenomena, offering versatile features to emulate and analyze complex systems.

For my research, the FEM played a pivotal role in creating a robust and accurate model for the simulation. The first step involved the careful setup of our material system within the software. After defining the precise parameters and boundary conditions, we subjected our modeled system to external vibrations. These vibrations are quintessential for studying the deformation behavior of materials under varying stress conditions. By introducing these disturbances, we were able to generate and capture images that displayed the deformations before and after the application of these vibrations.

Following the image acquisition phase, we delved into the crux of our study: Image registration. Image registration is an advanced technique that superimposes two or more images (in our case, the deformed and the initial images) to compare and analyze the differences. By employing sophisticated algorithms and techniques, we calculated the displacement experienced by the material under the applied vibration. This displacement, along with the known period, gave us insights into the shear modulus of the material.

Once we procured the shear modulus value via image registration, we entered the validation phase. It's essential to ensure that our derived results are not just accurate but also reliably

replicable. Given that the software has a strong foundation built on physics-based principles and mathematical rigor, its generated values served as a benchmark for our study. Hence, we juxtaposed our results against the elastic modulus we just inputted.

In scrutinizing the results, we accounted for the permissible margin of error. If our derived shear modulus were congruent with input values, within an acceptable range of discrepancy, it would underline the viability of our image registration technique. It would not only validate our approach but also highlight the potential of image registration as a reliable tool in such analyses. Here is the map of the 2D CT-based elastography simulation method, as shown in Figure 17.

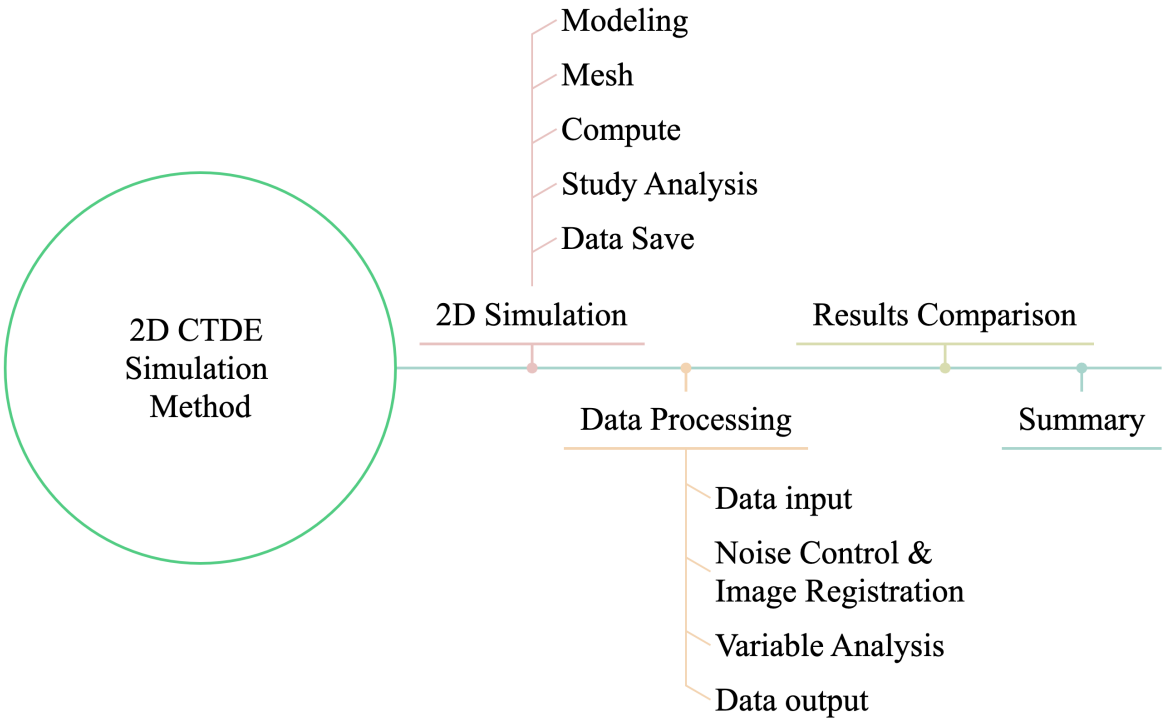

Figure 17. 2D CT-based Dynamic Elastography Simulation Method

4.2 2D Simulation

For our study, we turned to the software for constructing detailed structural models and for the subsequent analysis of those models, both in steady-state and transient scenarios.

Structural modeling, as the foundation of our simulation, required us to ensure that the material parameters, boundary conditions, and loadings were precisely defined. The meticulous setup ensured that our analysis would be grounded in realism and that the generated results would mimic true material behavior.

4.2.1 Modeling Geometry

In the initial stage of our research process, we prioritize the task of geometry modeling, which is a cornerstone in achieving precise results in our study. This stage is characterized by the design and establishment of a fundamental structure that will undergo further analysis in subsequent stages of our project. First, I used the primary canvas for our modeling endeavor, and I constructed a rectangle. This rectangle is defined with a width of 10 cm and a height of 20 cm. Within this rectangular framework, we proceed to introduce circular elements, positioned to create a cohesive and balanced geometric configuration. The circles are delineated with precise coordinates to ensure accurate placement within the rectangle. The centers of these circles are distinctly positioned at coordinates (5, -4), (5, -8), (5, -12), and (5, -16), the radius is 1 cm.

Subsequently, we undertake the process of unifying these individually crafted geometric elements into a cohesive whole, a procedure technically termed forming a "union." This step is pivotal, essentially merging the discrete entities to function as a single unit, fostering seamless interaction and coordination among the incorporated elements. The following table shows all the parameters of geometry in Table 1.

Table 1. Parameters of Geometry

Section	Circle	Rectangular
Coordinates	Center:(5, -4), (5, -8), (5, -12), (5, -16)	(0, 0), (10, 0), (0, -20), (10, -20)
Features	radius is 1 cm	width 10 cm, height 20 cm

4.2.2 Setting Material

In the materials setup phase of our simulation, the meticulous selection and allocation of materials to the different geometric constituents of our model hold a pivotal role. We begin this crucial step by designating the Intermediate-grade Invasive Ductal Carcinoma (IDC) as the material for the four circular entities within our geometry. This material exhibits a specific density of 1000 kg/m³, alongside mechanical properties characterized by Young's modulus of 10.4 kPa and a Poisson's ratio valued at 0.49.

Transitioning our focus to the encompassing rectangular section of our model, we opt for Normal fat tissue to serve as the foundational material. This choice is guided by the tissue's inherent properties which include a density marked at 1000 kg/m³, significantly differentiating it from the IDC material chosen for the circular entities. We made Young's modulus at 3.25 kPa, it has a different resistance to deformations compared to the IDC. Moreover, we made the Poisson's ratio at 0.49, a vital aspect in the forthcoming simulations. We know that if the Poisson’s ratio is bigger than 0.5 the material will be incompressible. This detailed materials setup, rooted in precise specifications, not only aids in creating a realistic simulation environment but also paves the way for accurate and reliable results in our research endeavor. The following table shows all the parameters of material in the Table 2.

Table 2. Parameters of Material

Section	Circle (material1)	Rectangular (material2)
Young's modulus	10.4kPa	3.25 kPa
Density	1000 kg/m³	1000 kg/m³
Poisson's ratio	0.49	0.49

4.2.3 Setting Solid Mechanics

In configuring the solid mechanics setup, a structured and well-strategized approach is paramount to achieve precise simulation results. Firstly, we fix the upper and lower boundaries of the rectangular framework in the y-direction. This entails immobilizing these edges to restrict movement and ensure stability during the simulation process, fostering a controlled environment for our experimental setup. Proceeding further, we impose a fixed constraint on the left boundary, wherein it is steadfast in both the x and y directions. This stipulation offers a firm anchorage, inhibiting any forms of displacement in the delineated directions, thereby establishing a rigid setup that mirrors real-life physical conditions meticulously. Following this, a significant action is undertaken on the right boundary where we introduce a vibration stimulus characterized by a sinusoidal wave. This wave is generated by a prescribed displacement with an amplitude of 0.05 cm and a frequency operating at 100 Hz, as shown in Figure 18, parting a dynamic aspect to our setup, creating conditions to study the resulting behaviors and responses under such stimulations.

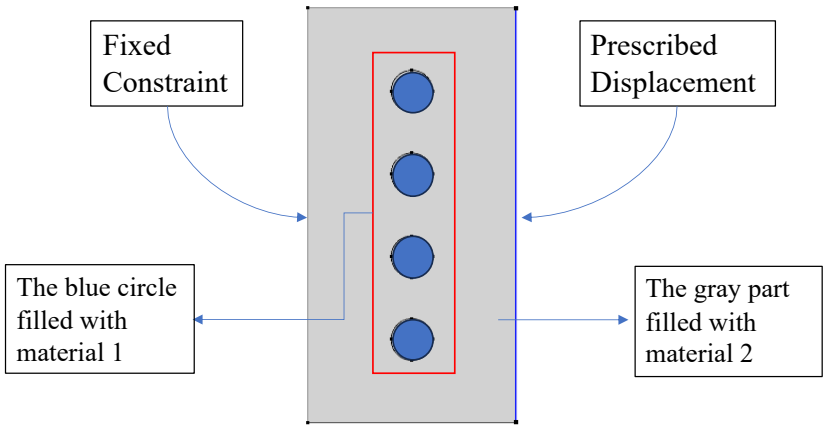

Figure 18. Experimental Model Details and Boundary Conditions

Moving towards the remaining boundaries, we designate them as free boundaries. This affords them to experience natural reactions without any predefined constraints, allowing for organic responses and interactions during the simulation. To conclude the setup, a meticulous verification process ensued to ensure chronological accuracy in the applied settings, thus cementing a foundation that is devoid of errors and stands robust for the forthcoming analytical procedures, fostering a pathway toward yielding precise and reliable outcomes in our study.

4.2.4 Setting Mesh

In the forthcoming step of our methodology, we proceed to mesh the diligently configured component using a well-defined strategy to achieve optimal results. We enlist the aid of a Physics-controlled mesh to facilitate this essential process, a choice grounded in its ability to align the mesh generation closely with the physical attributes and boundaries stipulated in our model, fostering a higher degree of fidelity in the representation.

In discerning the ideal element size for this endeavor, we settle on the 'fine' option, which implies a denser mesh grid, thereby allowing for a more detailed and nuanced capture of the varying physical phenomena during the simulation, ensuring a robust and detailed analysis later.

To bring this phase to completion, we activate the 'build all' function, a decisive step that effectively assembles the mesh, bringing together the individual elements in a cohesive manner, setting the stage for subsequent processes in our simulation study with a finely crafted mesh that stands ready to facilitate in-depth analyses and accurate outcomes.

4.2.5 Setting Compute

In the ensuing segment of our procedure, we direct our attention to configuring the compute segment, a pivotal section where the main analysis of our project occurs. The focal point here is initiating a transient study, a dynamic analysis that helps in understanding the time-varying phenomena occurring in our structure over a specified period.

We decide to dissect one complete cycle of the study into 200 increment steps, as shown in Figure 18, a strategy designed to foster a granulated inspection, thereby capturing intricate details at each juncture, which will potentially yield a rich dataset and a more refined understanding of the dynamic responses occurring within each fleeting moment of the cycle.

As we into this critical phase, our objective remains clear: to comprehensively explore the structural behaviors throughout one full cycle, leveraging the precision afforded by the meticulously segmented approach. Our anticipation is that, upon the completion of this analytical cycle, we will be equipped with a set of output results that offer deep insights and a detailed overview of the transient phenomena under study, laying a solid base for the ensuing discussions and conclusions in our research endeavor.

4.2.6 Study Analysis

Upon completion of the model setup, we proceeded with transient analysis. The transient analysis delved into the material's reactions to time-varying conditions, offering a dynamic

perspective of its behavior. The analyses yielded visual results: deformation images, as shown in Figure 19.

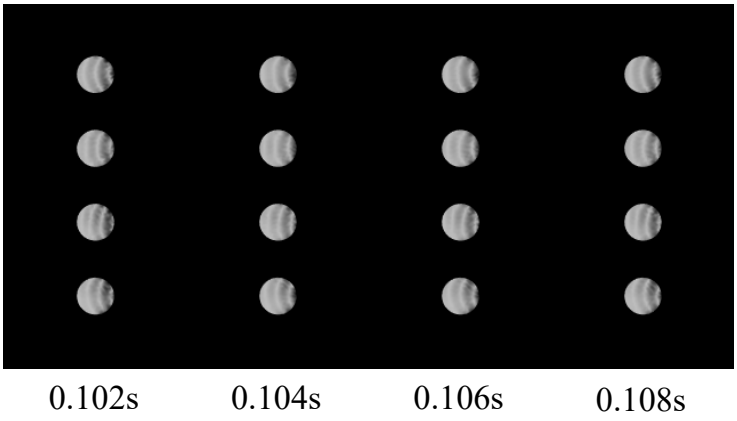

Figure 19. The Resulting Deformation Diagrams

At this juncture, we diligently proceed to manipulate the deformation diagrams derived from the transient analysis, setting a goal to represent them as grayscale images. This transformation not only facilitates a nuanced visualization but also aids in a meticulous analysis by emphasizing the varying degrees of deformation distinctly. Following this detailed representation transformation, we systematically output and save these refined grayscale diagrams, ensuring they are preserved for the subsequent analytical processes and discussions in our study.

4.2.7 Data Save

Upon utilizing the software for our computations, we distilled our findings into a set of deformation maps, conveniently stored as PNG files to facilitate subsequent data retrieval. These four illustrative images chronicle the transformation of our system in four distinct phases within a single cycle. Such visual representations serve not just as a testament to the system's dynamic evolution but also set the stage for the intricate data processing we'll be embarking on in the subsequent sections.

4.3 Data Processing

In this chapter, we navigate the intricate process of using the results, steering them toward our targeted outcomes. Using MATLAB, we extract graphical data, setting the stage for subsequent manipulations. The 'Demons Method' is our chosen instrument for registering the acquired set of images. Our journey doesn't end there; from the registration, we derive deformation parameters, culminating in the creation of a displacement map. This paves the way for the final production of a modulus map.

4.3.1 Data Input

In this stage, images derived from simulation, organized chronologically, are stored in MATLAB arrays. This methodical approach forms a repository of variables, streamlining the subsequent processes, particularly facilitating the imminent registration tasks.

4.3.2 Noise Control and Image Registration

For noise reduction in our images, we implemented both the Butterworth filter and the Gaussian filter. In terms of image registration, I utilized the Demons algorithm, aligning the captured image data chronologically. Within a single cycle, the four designated "moving" images were systematically aligned with the initial, undeformed "stable" image. Through iterative experimentation, I meticulously fine-tuned the registration parameters to meet our precision criteria. After the registration, we retained the pivotal variables used, constructing a robust database that proved instrumental in subsequent calculations for displacement and modulus maps.

4.3.3 Variable Analysis

In this step, our focus narrows to meticulous computations derived from variables obtained during registration, culminating in the generation of a displacement amplitude map, as shown in Figure 20.

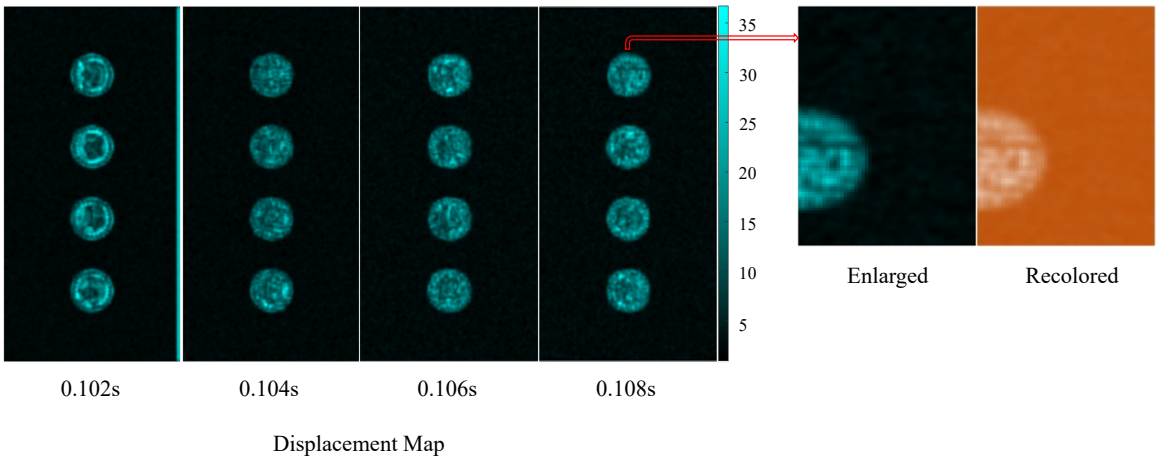

Figure 20. Displacement Amplitude Map

Given that each variable encapsulates data corresponding to the magnitude of deformation along the x and y axes for each pixel within an image, we can calculate the overall displacement magnitude using the distance formula. By mapping these calculations back to their respective pixels, we produce a comprehensive displacement map. Armed with the displacement magnitude per point and cognizant of the time interval involved in inducing said displacement, we possess the necessary elements to calculate wave speed. Invoking the principles governing the propagation of elastic waves in solids, we can approximate the elastic modulus. This process ends in the form of an elastic modulus map, which is our aim, as shown in Figure 21. Upon scrutinizing the elastic modulus map derived above, the results depicted within confirm that the elastic modulus of the circular section ranges between 10,000 and 11,000, while the remaining areas vary from 3,000 to 4,000. This result is in harmony with the data inputs we utilized during our modeling process.

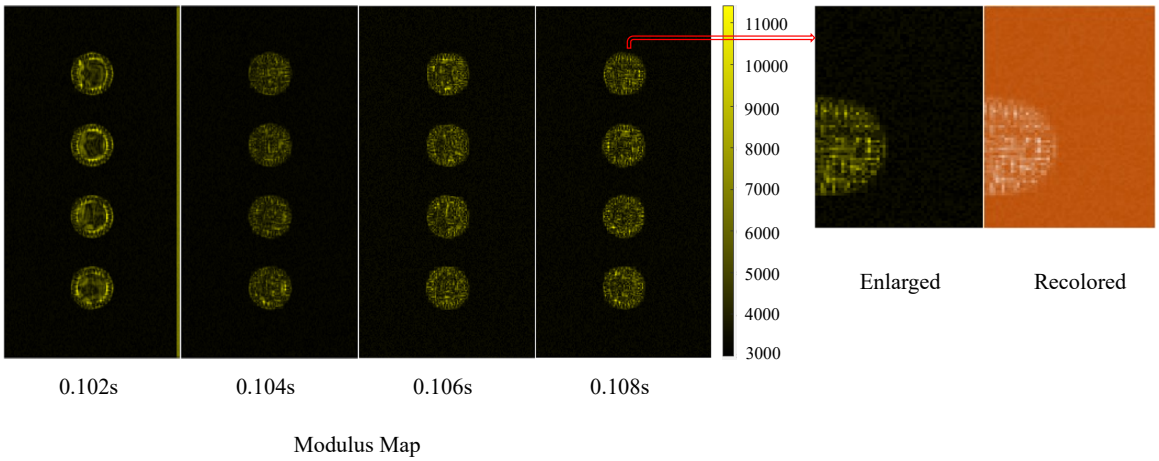

Figure 21. Elastic Modulus Map

4.3.4 Data Output

In this step, we chronologically catalog the obtained displacement and modulus maps, preserving them both as PNG images and structured data tables corresponding to specific time points.

4.4 Results Comparison

Upon obtaining our refined images, we embarked on a comparative study. The displacement maps and Young's modulus maps obtained post-registration were juxtaposed against the initial results from the simulation. This comparative analysis was instrumental in identifying the efficacy of our approach. A key revelation from this simulation was the ability of the refined maps to distinguish various regions or chunks within the material, highlighting differential behavior and properties. Through this methodology, we can calculate the modulus data that we've inputted.

4.5 Summary

The results we have achieved, underscore the viability of our method: applying dynamic vibrations to an object, capturing its deformation, and then processing this data to derive its elastic modulus map. This approach is fundamentally rooted in the science of elastography, a validated scientific technique, affirming its scientific integrity. This non-invasive probing allows us to map the elasticity properties of soft tissues.

At its core, our study has illuminated the potential of leveraging simulations combined with image processing techniques to achieve elastography imaging. The image acquisition phase in our study was simulated using software; however, in a practical scenario, high-speed CT imaging equipment would be employed. Nevertheless, the subsequent image processing phase remains consistent. Through adept data manipulation, we can obtain an elasticity feature map showcasing varying modulus distributions. The success of this experiment hints at its potential to differentiate between healthy and afflicted tissues in medical contexts. In real-world applications, the deformation imagery of the test object can be directly captured via CT. Conventional CT images currently offer only basic shape and shading information. Through 2D CTDE, we can achieve more detailed 2D elastography images with clearer boundaries, potentially amplifying the efficacy of current diagnostic procedures.

Chapter 5. 3D CT-based Dynamic Elastography Simulation

Building upon the foundational understanding garnered from our two-dimensional simulations, we've embarked on an expansion of our research to encompass the intricacies of a three-dimensional realm. Given that both 2D CT and 3D CT serve the role of capturing images in this imaging technique, COMSOL Multiphysics remains our choice simulation tool. Utilizing this software, we've acquired three-dimensional deformation maps at varying transient moments within a single vibration cycle, which subsequently facilitated our modulus map computations. In this chapter, we delve deeply into the nuances of this simulation process, showcasing the significant outcomes of our endeavor and focusing on every intricate detail involved, as shown in Figure 22.

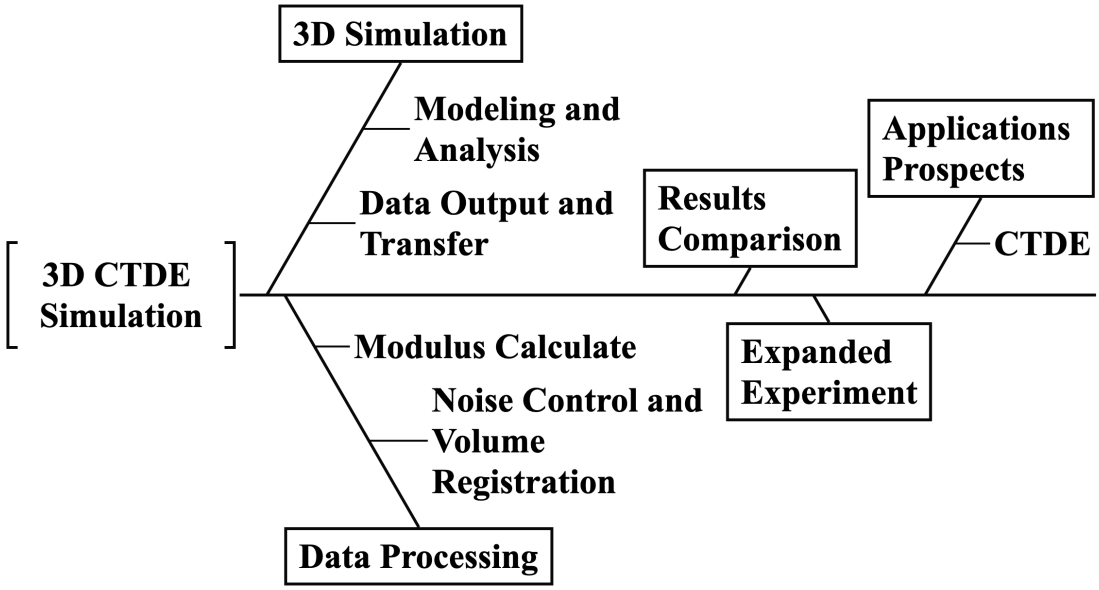

Figure 22. 3D CT-based Dynamic Elastography Simulation Method

5.1 Modeling and Analysis

In computational investigations, platforms like 3D modeling offer the means to visualize and dissect intricate structures and their reactions under diverse scenarios. To venture further, we construct a cubic 3D model measuring 10cm x 10cm x 10cm. Located within the cube is a sphere with a diameter of 1 centimeter. The following table shows all the parameters of material in the Table 3.

Table 3. Parameters of Model

Section	Sphere (material1)	Cube (material2)
Coordinates	Center (5, -5,5)	Corner (0,10,0)
Features	radius is 1 cm	width 10 cm, height 10 cm, depth 10 cm
Young's modulus	10.4 kPa	3.25 kPa
Density	1000 kg/m³	1000 kg/m³
Poisson’s ratio	0.49	0.49

To mirror real CT experiment scenarios and assess the model's reactions, one facet of the cube was securely anchored, serving as an anchor point and stabilizing base. Across from this anchored surface, a sinusoidal wave is generated by a prescribed displacement with an amplitude of 0.05 cm and a frequency operating at 100 Hz. This approach sought to expose the model to vibration scenarios to monitor its diverse reactions, as shown in Figure 23.

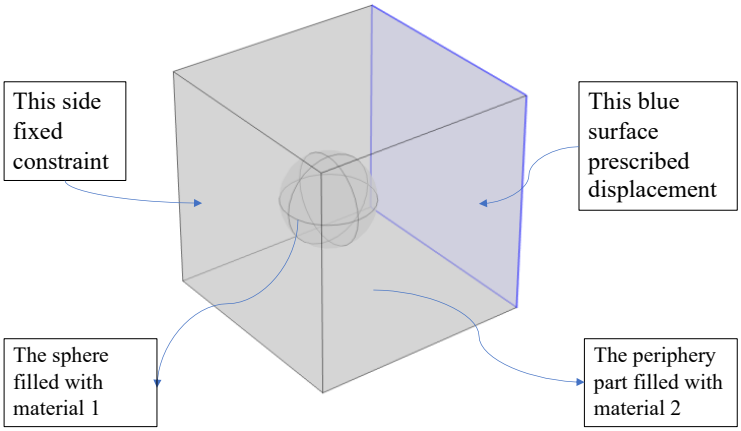

Figure 23. Model Details and Boundary Conditions

Harnessing the time-dependent simulation, we could deduce the model's evolving reactions. The software churned out nuanced depictions of the model's shape alterations, documenting the subtle transitions and structural shifts due to the induced oscillations. Moreover, maps illustrating displacements were crafted, shedding light on the shifts in position and movements across various model sections, with a keen spotlight on the internal spherical segment. These detailed shape and displacement depictions carry significant weight, especially for the registration.

5.2 Data Output and Transfer

Upon obtaining results through the software, we extracted a set of deformation maps stored in the VTU format, representing three-dimensional model diagrams. These four VTU models mirror the deformation of the entire system at four distinct moments within a single cycle. Given MATLAB's limitation in natively reading 3D data files in subsequent steps, it becomes imperative to convert these data files into a format readable by MATLAB. In my simulation, I used the VTU format to save it. Leveraging Python, I've transitioned the data into the CSV

format, subsequently executing linear interpolation on the data within the CSV files. This transformation produces a well-structured three-dimensional array, setting the stage for the ensuing registration processes.

5.3 Noise Control and Volume Registration

In the progression of our research, the utilization of the Demon method played an instrumental role in the registration step. In this stage, we employ the mentioned theory to execute volume registration on the captured transient models. The primary objective is to discern the relative transformation values between these models. More precisely, we can calculate the coordinate shift for each point by non-rigid registration.

Through this registration process, we are adeptly equipped to quantify the displacements in the X, Y, and Z directions. This not only furnishes us with an intricate view of positional changes but also empowers us to compute the magnitude of displacement experienced by each point within the model. Moreover, discerning the magnitude of displacement for each point holds considerable merit. It not only provides insight into the dynamic behavior of the model structure throughout the cycle but also paves the way for subsequent modulus analysis. Armed with this data, calculating the modulus becomes considerably more achievable.

5.4 Modulus Calculate

Utilizing the findings from the registration analysis, we adeptly extracted a comprehensive map delineating the magnitudes of displacement changes within the model. By considering the magnitude of these shifts, the time span of these alterations, as well as the frequency and amplitude of the vibrations inducing such changes, we deduced the system's elastic modulus. It's noteworthy that the contours of the inner sphere within the cube are distinctly outlined in the

visualization of this modulus map, as shown in Figure 24. Examining the elastic modulus map, the depicted outcomes verify that the material within the circular region exhibits an elastic modulus ranging from 10,000 to 11,000. In contrast, the modulus values of the other areas lie between 3,000 and 4,000. These findings correspond seamlessly with the data inputs we established during our modeling phase.

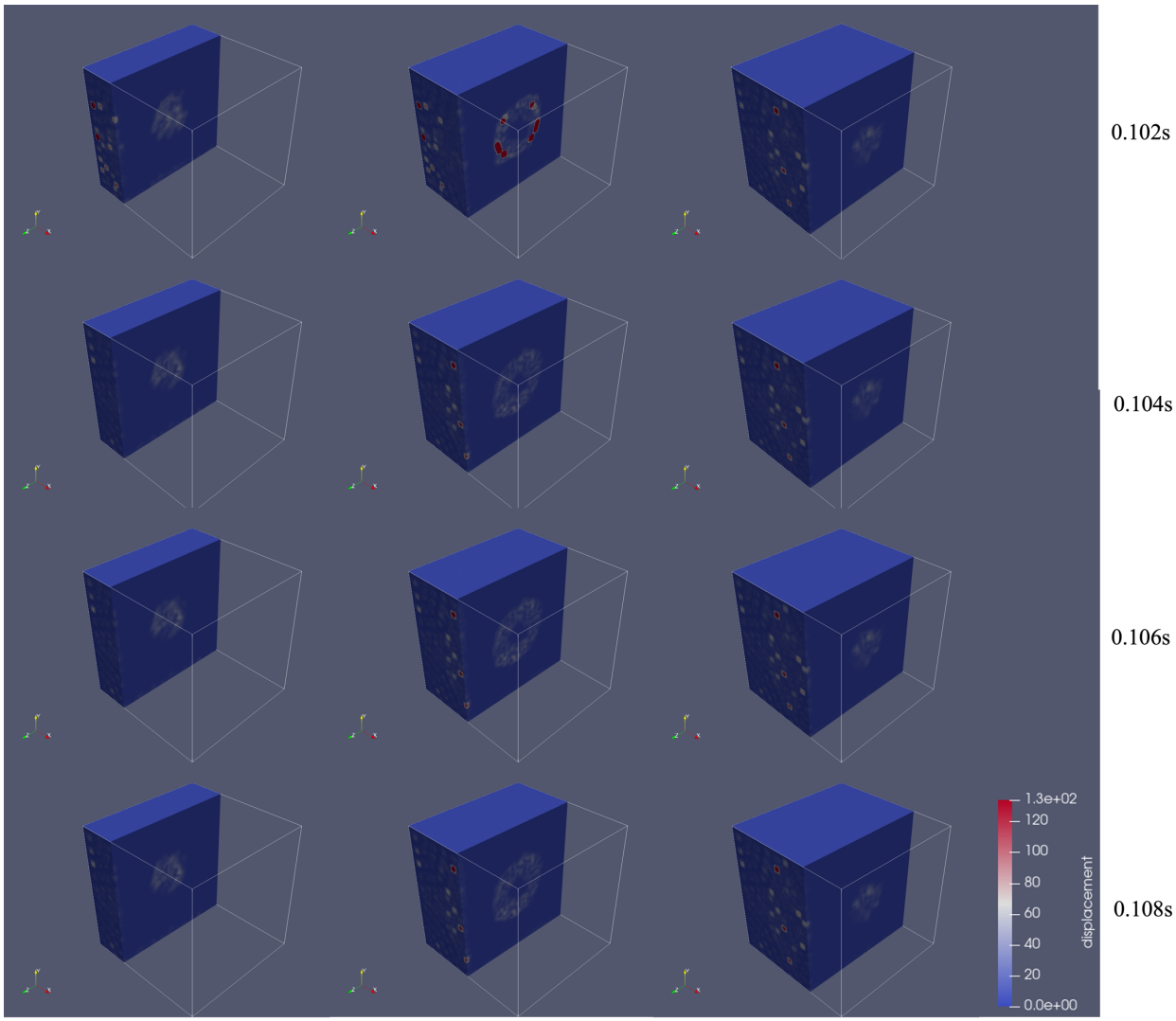

X=30mm X=50mm X=70mm

Displacement Map

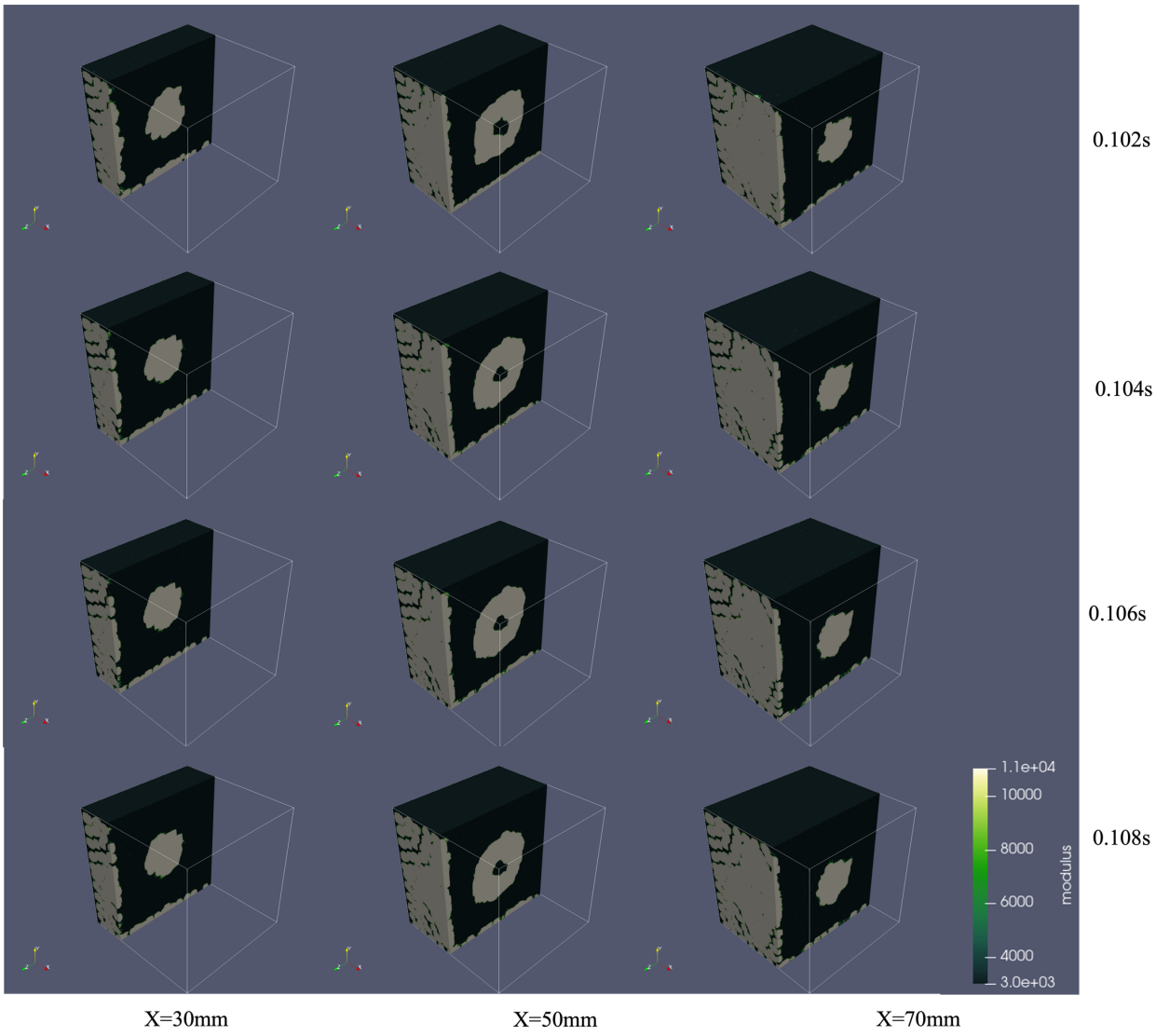

Figure 24. Displacement and Modulus Map

5.5 Results Comparison

In this period, we employed 3D viewing software to dissect the acquired system modulus model into several distinctive feature slices for in-depth analysis. We have chosen several specific slices, each representing a unique cross-sectional modulus distribution of the system.

Through visual comparative analysis, we can visualize the distribution and values of the modulus at different depths within the 3D model.

The crux of this step depends on determining whether the 3D simulation can genuinely emulate the successes seen in 2D, thus achieving the desired outcomes. In essence, this stage serves not only as validation but also as a pivotal juncture to test our underlying assumptions. If we can generate a system modulus map with clear boundaries in a three-dimensional simulation, following the steps of the two-dimensional experiment, it would attest to its potential applicability in 3D CTDE.

Fortunately, our experimental findings demonstrate that this method successfully generates modulus distribution maps whose boundaries are well-defined, with the images precisely delineating the properties of different tissues. In the modulus map mentioned earlier, by setting aside some boundary details, we observe that the calculated modulus values align well with the data inputs formulated during the experimental design phase.

5.6 Expanded Experiment

In the preceding experiment, we utilized a perfect sphere positioned at the center of a cube. Now, we're placing an irregular object within a rectangular matrix and replicating the same experimental steps. If similar outcomes are achieved, it will substantially reinforce the credibility and persuasiveness of our experimental methods and underlying principles.

We embedded a polymeric material into a phantom composed of a silicone matrix for our simulation. Owing to the irregular shape of the rubber, we employed a CT scanner during the modeling process to acquire its three-dimensional representation. This 3D model was then imported into COMSOL, facilitating the subsequent steps of simulation analysis. Detailed parameters of this experiment are presented in Table 4 [69].

Table 4. Parameters of Model

Section	Rubber (material1)	Silicone matrix (material2)
Features	Scanned by CT	width 30 mm, height 28 mm, depth 20 mm
Young's modulus	2610 kPa	2140 kPa
Density	2850 kg/m³	1050 kg/m³
Poisson's ratio	0.3	0.3

Once our modeling was finalized, we were able to observe a 3D view of the entire model, as shown in Figure 25.

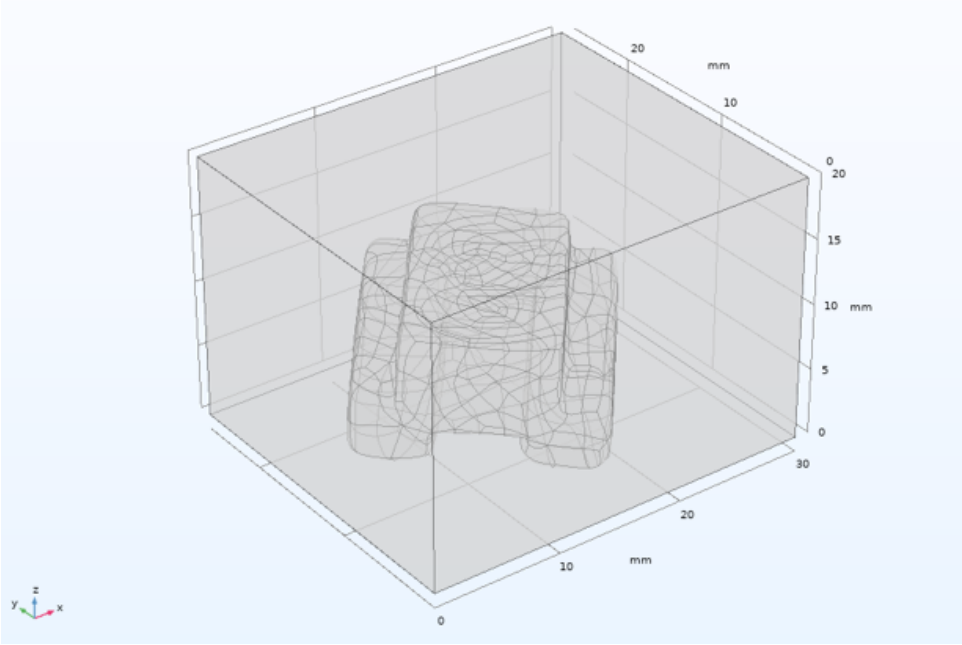

Figure 25. Experimental Model Shape and Coordinate Information

To facilitate detailed examination in subsequent stages, we conducted a sectional display by slicing the model at specific x-values of 6mm, 12mm, 18mm, and 24mm, as shown in Figure 26.

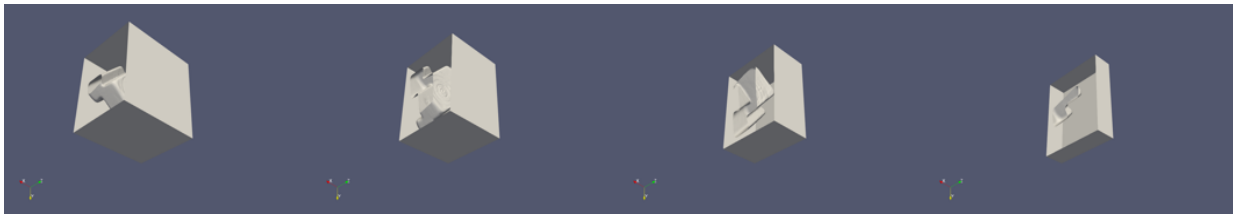

X=6mm X=12mm X=18mm X=24mm

Figure 26. Slices of the Experimental Model in the X-axis Direction

Implementing our experimental procedure and data processing techniques, we arrived at the following findings, displacement map and modulus map, as shown in Figure 27. We focus on the shape we can detect in the object, so we can set aside the edge effects in the modulus map. It becomes apparent that the shape of the rubber is distinctly highlighted, with values ranging between 2400kpa and 2600kpa. Meanwhile, the Silicone matrix registers between 1900kpa and 2100kpa. Such outcomes correspond well with our initial data inputs, indicating that our methodology is characterized by its generality and potential for broader applicability.

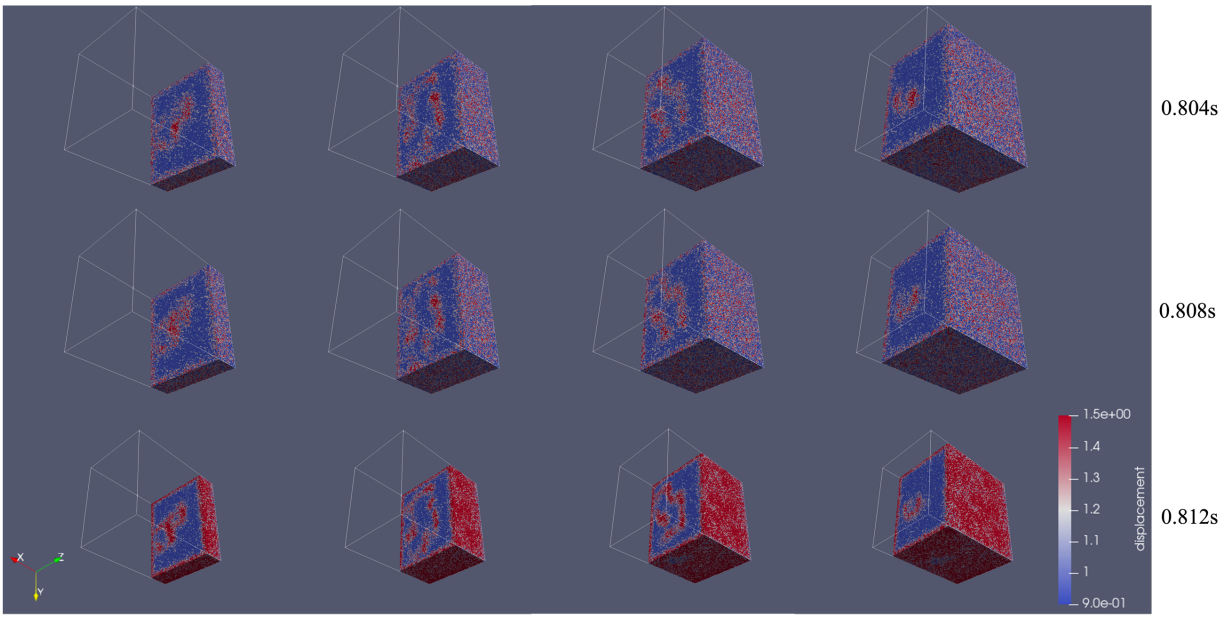

X=6mm X=12mm X=18mm X=24mm

(a)

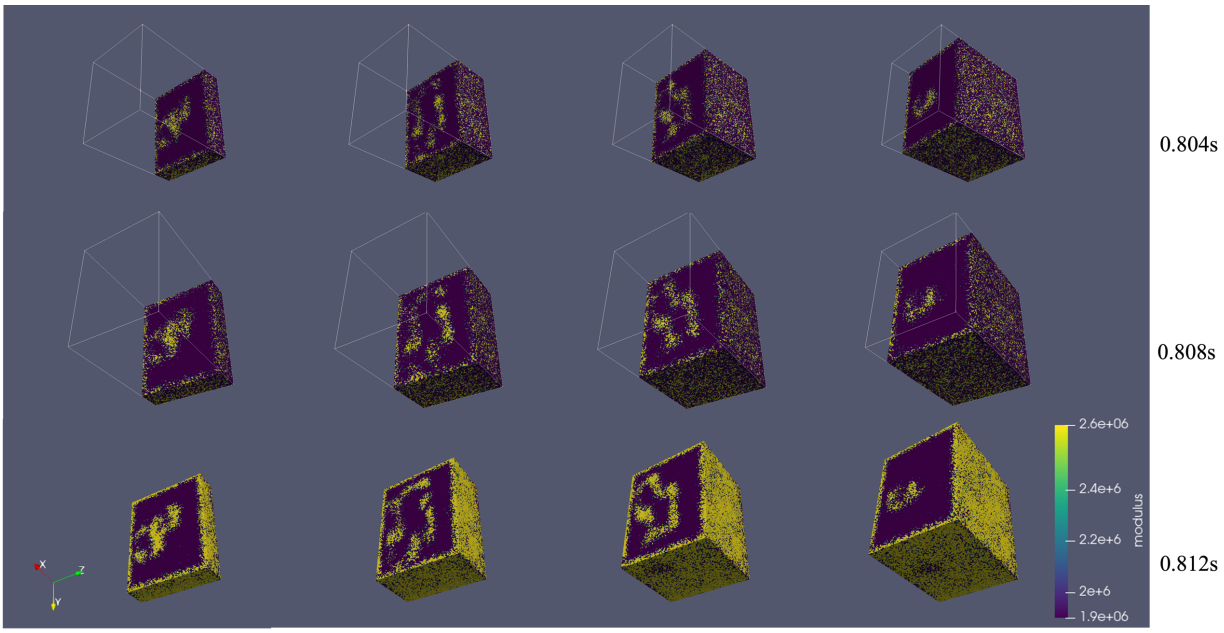

Figure 27. (a) is the displacement map and (b) is the modulus map

5.7 Prospective Applications in CTDE

After rigorous validation of the 3D simulation outcomes, it was evident that the clarity and feasibility of the images obtained were on par with the 2D results counterparts. As these simulations are validated, we propose that the CTDE has a compelling prospect. It can be anticipated that employing the same approach for acquiring CT images in the real world and subsequent registration could realize the desired outcomes.

The 2D simulation and 3D simulation research expanded the theoretical feasibility of elastography from a two-dimensional plane to a three-dimensional space. The profound insights garnered from this endeavor not only attest to the robustness of our methodology but also underscore its potential for real-world application. With the prospective advancement of actual CTDE research, these simulations might soon manifest into reality. By doing so, we're poised to

shepherd this innovative approach from its conceptual phase to the forefront of practical research and application in the medical imaging domain.

Chapter 6. Conclusions

The goal of this research was to implement three-dimensional CT-based dynamic elastography by harnessing aerodynamic vibration combined with image processing methodologies to deduce the elastic modulus of materials. Elastography primarily deduces the mechanical properties of materials by observing their deformations, holding significant implications in both engineering and medical realms.

Through simulation facilitated by the software, we successfully garnered deformation maps under the dynamic vibration of the test subjects. These deformation illustrations depict the material's behavioral changes under vibrational influences, laying the base for ensuing calculations of elastic modulus.

Subsequent image analyses were conducted using MATLAB, which encompassed noise mitigation, image registration, and variable analysis. Utilizing Butterworth and Gaussian filters, we adeptly minimized image noise and smoothened the edges. By employing the Demons algorithm for image registration, we managed to align the moving images with the steady ones, securing an accurate displacement field. Delving into this displacement map, we determined both the magnitude of displacement and the elastic modulus.

Our findings indicate that the combination of aerodynamic vibrations with image processing techniques allows for successful extrapolation of the material's elastic modulus. Such methodologies carry latent application value in the biomedical domain, especially in tissue diagnostics and anomaly detection, akin to MRE. It can be used for diagnostic measurements of breast cancer, furnishing the advantage of attaining elastography maps within a shorter time frame as opposed to MRE.

Given that two-dimensional CTDE captures only one directional elastic distribution, dedicated to three-dimensional exploration would enable us to perceive the modulus distribution throughout the entirety of the 3D object. This depth of information can provide a more intricate understanding of heterogeneities within the object. To materialize this vision, a cubic 3D model was constructed, with sinusoidal vibrations administered to observe model responses. Transient simulations captured nuanced changes in model shape and structural transitions. Simulation outcomes were exported in 3D data format and converted to MATLAB readable CSV format using Python. Through volumetric registration techniques, we discerned coordinate shifts between distinct deformation images, leading to the retrieval of displacement magnitudes and elastic modulus.

By comparing two-dimensional and three-dimensional simulation, the difference is obvious. While 2D simulations proffer rapid calculations and a simplified model, they fail to encapsulate the holistic deformation behavior of the object. In contrast, 3D simulations offer a more precise and elaborate depiction of model behavior, albeit at a higher computational cost.

In summation, elastography emerges as a potential method in medical diagnostics. While ultrasound elastography and magnetic resonance elastography have been substantially integrated into clinical scenarios with pronounced success, CTDE, as a budding technique we proposed, offers deep penetration capabilities and high-resolution advantages, introducing fresh diagnostic possibilities.

Future research endeavors should delve more profoundly into elastography techniques spanning a multitude of material types and different boundary conditions. The creation of a database dedicated to transformation parameters is essential to refine registration details meticulously. An exploration merging varied vibrational frequencies, amplitudes, and imaging

strategies could lay the foundation for enhanced computational efficacy and crisper elastography visuals. Considerations for employing CTDE methods in real-world settings should also be pondered, encompassing topics like the synchronized control of aerodynamic vibrations and strategies for radiation dosage management. Another critical aspect to inspect would be the noise reduction in CTDE, aiming to augment data processing accuracy. In essence, empirical research's nuanced insights will be invaluable. Such detailed data might not only broaden the technique's real-world applicability but also elevate its efficacy and impact in clinical settings.

References

[1] Siegel, R. L., Miller, K. D., Wagle, N. S., & Jemal, A. (2023). Cancer statistics, 2023. Ca Cancer J Clin, 73(1), 17-48.

[2] Samani, A., Zubovits, J., & Plewes, D. (2007). Elastic moduli of normal and pathological human breast tissues: an inversion-technique-based investigation of 169 samples. Physics in medicine & biology, 52(6), 1565.

[3] Ophir, J., Cespedes, I., Ponnekanti, H., Yazdi, Y., & Li, X. (1991). Elastography: a quantitative method for imaging the elasticity of biological tissues. Ultrasonic imaging, 13(2), 111-134.

[4] Muthupillai, R., Lomas, D. J., Rossman, P. J., Greenleaf, J. F., Manduca, A., & Ehman, R. L. (1995). Magnetic resonance elastography by direct visualization of propagating acoustic strain waves. science, 269(5232), 1854-1857.

[5] Hamilton, T. J., Bailat, C., Gehring, S., Laperle, C. M., Wands, J., Rose-Petruck, C., & Diebold, G. J. (2009). X-ray elastography: Modification of x-ray phase contrast images using ultrasonic radiation pressure. Journal of Applied Physics, 105(10).

[6] Kamezawa, C., Numano, T., Kawabata, Y., Kanetaka, H., Furuya, M., Yokota, K., ... & Yashiro, W. (2020). X-ray elastography by visualizing propagating shear waves. Applied Physics Express, 13(4), 042004.

[7] Garra, B. S., Krasner, B. H., Horii, S. C., Ascher, S., Mun, S. K., & Zeman, R. K. (1993). Improving the distinction between benign and malignant breast lesions: the value of sonographic texture analysis. Ultrasonic imaging, 15(4), 267-285.

[8] Loomba, R., Wolfson, T., Ang, B., Hooker, J., Behling, C., Peterson, M., ... & Sirlin, C. (2014). Magnetic resonance elastography predicts advanced fibrosis in patients with nonalcoholic fatty liver disease: a prospective study. Hepatology, 60(6), 1920-1928.

[9] Mariappan, Y. K., Glaser, K. J., & Ehman, R. L. (2010). Magnetic resonance elastography: a review. Clinical anatomy, 23(5), 497-511.

[10] Röntgen, W. C. (1896). On a new kind of rays. Science, 3(59), 227-231.

[11] Ginat, D. T., & Gupta, R. (2014). Advances in computed tomography imaging technology. Annual review of biomedical engineering, 16, 431-453.

[12] Graff, K. F. (2012). Wave motion in elastic solids. Courier Corporation.

[13] Sadd, M. H. (2009). Elasticity: theory, applications, and numerics. Academic Press.

[14] Parker, K. J., Doyley, M. M., & Rubens, D. J. (2010). Imaging the elastic properties of tissue: the 20 year perspective. Physics in medicine & biology, 56(1), R1.

[15] Bamber, Jeffrey, et al. "EFSUMB guidelines and recommendations on the clinical use of ultrasound elastography. Part 1: Basic principles and technology." Ultraschall in der Medizin-European Journal of Ultrasound 34.02 (2013): 169-184.

[16] Palmeri, M. L., & Nightingale, K. R. (2011). What challenges must be overcome before ultrasound elasticity imaging is ready for the clinic?. Imaging in medicine, 3(4), 433.

[17] Tanter, M., & Fink, M. (2014). Ultrafast imaging in biomedical ultrasound. IEEE transactions on ultrasonics, ferroelectrics, and frequency control, 61(1), 102-119.

[18] Shiina, Tsuyoshi, et al. "WFUMB guidelines and recommendations for clinical use of ultrasound elastography: Part 1: basic principles and terminology." Ultrasound in medicine & biology 41.5 (2015): 1126-1147.

[19] O'Donnell, M., Skovoroda, A. R., Shapo, B. M., & Emelianov, S. Y. (1994). Internal displacement and strain imaging using ultrasonic speckle tracking. IEEE transactions on ultrasonics, ferroelectrics, and frequency control, 41(3), 314-325.

[20] Manduca, A., Oliphant, T. E., Dresner, M. A., Mahowald, J. L., Kruse, S. A., Amromin, E., ... & Ehman, R. L. (2001). Magnetic resonance elastography: non-invasive mapping of tissue elasticity. Medical image analysis, 5(4), 237-254.

[21] Green, M. A., Bilston, L. E., & Sinkus, R. (2008). In vivo brain viscoelastic properties measured by magnetic resonance elastography. NMR in Biomedicine: An International Journal Devoted to the Development and Application of Magnetic Resonance In vivo, 21(7), 755-764.

[22] Yin, M., Talwalkar, J. A., Glaser, K. J., Manduca, A., Grimm, R. C., Rossman, P. J., ... & Ehman, R. L. (2007). Assessment of hepatic fibrosis with magnetic resonance elastography. Clinical Gastroenterology and hepatology, 5(10), 1207-1213.

[23] Kruse, S. A., Smith, J. A., Lawrence, A. J., Dresner, M. A., Manduca, A. J. F. G., Greenleaf, J. F., & Ehman, R. L. (2000). Tissue characterization using magnetic resonance elastography: preliminary results. Physics in Medicine & Biology, 45(6), 1579.

[24] Romano, A. J., Bucaro, J. A., Ehnan, R. L., & Shirron, J. J. (2000). Evaluation of a material parameter extraction algorithm using MRI-based displacement measurements. IEEE transactions on ultrasonics, ferroelectrics, and frequency control, 47(6), 1575-1581.

[25] Venkatesh, S. K., Yin, M., & Ehman, R. L. (2013). Magnetic resonance elastography of liver: technique, analysis, and clinical applications. Journal of magnetic resonance imaging, 37(3), 544-555.

[26] Ringleb, S. I., Chen, Q., Lake, D. S., Manduca, A., Ehman, R. L., & An, K. N. (2005). Quantitative shear wave magnetic resonance elastography: comparison to a dynamic shear

material test. Magnetic Resonance in Medicine: An Official Journal of the International Society for Magnetic Resonance in Medicine, 53(5), 1197-1201.

[27] Huwart, L., Sempoux, C., Vicaut, E., Salameh, N., Annet, L., Danse, E., ... & Van Beers, B. E. (2008). Magnetic resonance elastography for the noninvasive staging of liver fibrosis. Gastroenterology, 135(1), 32-40.

[28] Venkatesh, S. K., Yin, M., Glockner, J. F., Takahashi, N., Araoz, P. A., Talwalkar, J. A., & Ehman, R. L. (2008). Magnetic resonance elastography of liver tumors-preliminary results. AJR. American journal of roentgenology, 190(6), 1534.

[29] Kim, J. G., Aowlad Hossain, A. B. M., Shin, J. H., & Lee, S. Y. (2012). Calculation of strain images of a breast-mimicking phantom from 3D CT image data. Medical Physics, 39(9), 5469-5478.

[30] Kim, J. G., Park, S. E., & Lee, S. Y. (2014). X-ray strain tensor imaging: FEM simulation and experiments with a micro-CT. Journal of X-Ray Science and Technology, 22(1), 63-75.

[31] Sutphin, C., Olson, E., Motai, Y., Lee, S. J., Kim, J. G., & Takabe, K. (2019). Elastographic tomosynthesis from X-ray strain imaging of breast cancer. IEEE Journal of Translational Engineering in Health and Medicine, 7, 1-12.

[32] Photonics Science. (2023, 9,14). X-ray sCMOS 16MP Detector. Photonics Science. https://photonicscience.com/products/x-ray-cameras/x-ray-scmos-16mp-detector/

[33] Butterworth, S. (1930). On the theory of filter amplifiers. Wireless Engineer, 7(6), 536-541.

[34] Oppenheim. (1999). Discrete-time signal processing /. Prentice Hall,.

[35] Rabiner, L. R., & Gold, B. (1975). Theory and application of digital signal processing. Englewood Cliffs: Prentice-Hall.

[36] Lyons, R. G. (2010). Digital data formats and their effects. Understanding digital signal processing, Pearson Education Inc., Ann Arbor, MI.

[37] Gonzalez. (2009). Digital image processing /. Addison-Wesley Pub Co, Advanced Book Program,.

[38] Jain, A. K. (1989). Fundamentals of digital image processing. Prentice-Hall, Inc..

[39] Lim, J. S. (1990). Two-dimensional signal and image processing. Englewood Cliffs.

[40] Canny, J. (1986). A computational approach to edge detection. IEEE Transactions on pattern analysis and machine intelligence, (6), 679-698.

[41] Bovik, A. C. (2010). Handbook of image and video processing. Academic press.

[42] Haralick, R. M. (1987). Digital step edges from zero crossing of second directional derivatives. In Readings in computer vision (pp. 216-226). Morgan Kaufmann.

[43] Marr, D., & Hildreth, E. (1980). Theory of edge detection. Proceedings of the Royal Society of London. Series B. Biological Sciences, 207(1167), 187-217.

[44] Duda, R. O., & Hart, P. E. (1973). Pattern classification and scene analysis (Vol. 3, pp. 731-739). New York: Wiley.

[45] Szeliski, R. (2022). Computer vision: algorithms and applications. Springer Nature.

[46] Pratt, W. K. (2007). Digital image processing: PIKS Scientific inside (Vol. 4). Hoboken, New Jersey: Wiley-interscience.

[47] Maini, R., & Aggarwal, H. (2009). Study and comparison of various image edge detection techniques. International journal of image processing (IJIP), 3(1), 1-11.

[48] Sonka, M., Hlavac, V., Boyle, R., Sonka, M., Hlavac, V., & Boyle, R. (1993). Image pre-processing. Image processing, analysis and machine vision, 56-111.

[49] Bankman, I. (Ed.). (2008). Handbook of medical image processing and analysis. Elsevier.

[50] Roberts, R. A., & Mullis, C. T. (1987). Digital signal processing. Addison-Wesley Longman Publishing Co., Inc..

[51] Roberts, M. J. (2004). Signals and systems: analysis using transform methods and MATLAB. (No Title).

[52] Beauchemin, S. S., & Barron, J. L. (1995). The computation of optical flow. ACM computing surveys (CSUR), 27(3), 433-466.

[53] Lucas, B. D., & Kanade, T. (1981, August). An iterative image registration technique with an application to stereo vision. In IJCAI'81: 7th international joint conference on Artificial intelligence (Vol. 2, pp. 674-679).

[54] Horn, B. K., & Schunck, B. G. (1981). Determining optical flow. Artificial intelligence, 17(1-3), 185-203.

[55] Farnebäck, G. (2003). Two-frame motion estimation based on polynomial expansion. In Image Analysis: 13th Scandinavian Conference, SCIA 2003 Halmstad, Sweden, June 29–July 2, 2003 Proceedings 13 (pp. 363-370). Springer Berlin Heidelberg.

[56] Dosovitskiy, A., Fischer, P., Ilg, E., Hausser, P., Hazirbas, C., Golkov, V., ... & Brox, T. (2015). Flownet: Learning optical flow with convolutional networks. In Proceedings of the IEEE international conference on computer vision (pp. 2758-2766).

[57] Piegl, L., & Tiller, W. (1996). The NURBS book. Springer Science & Business Media.

[58] Rueckert, D., Sonoda, L. I., Hayes, C., Hill, D. L., Leach, M. O., & Hawkes, D. J. (1999). Nonrigid registration using free-form deformations: application to breast MR images. IEEE transactions on medical imaging, 18(8), 712-721.

[59] Rohde, G. K., Aldroubi, A., & Dawant, B. M. (2003). The adaptive bases algorithm for intensity-based nonrigid image registration. IEEE transactions on medical imaging, 22(11), 1470-1479.

[60] Klein, A., Andersson, J., Ardekani, B. A., Ashburner, J., Avants, B., Chiang, M. C., ... & Parsey, R. V. (2009). Evaluation of 14 nonlinear deformation algorithms applied to human brain MRI registration. Neuroimage, 46(3), 786-802.

[61] Kybic, J., & Unser, M. (2003). Fast parametric elastic image registration. IEEE transactions on image processing, 12(11), 1427-1442.

[62] Zienkiewicz, O. C., & Taylor, R. L. (2005). The finite element method for solid and structural mechanics. Elsevier.

[63] Modersitzki, J. (2009). FAIR: flexible algorithms for image registration. Society for Industrial and Applied Mathematics.

[64] Miga, M. I., Roberts, D. W., Kennedy, F. E., Platenik, L. A., Hartov, A., Lunn, K. E., & Paulsen, K. D. (2001). Modeling of retraction and resection for intraoperative updating of images. Neurosurgery, 49(1), 75-85.

[65] Ferrant, M., Nabavi, A., Macq, B., Black, P. M., Jolesz, F. A., Kikinis, R., & Warfield, S. K. (2002). Serial registration of intraoperative MR images of the brain. Medical image analysis, 6(4), 337-359.

[66] Shen, D., Wu, G., & Suk, H. I. (2017). Deep learning in medical image analysis. Annual review of biomedical engineering, 19, 221-248.

[67] Sotiras, A., Davatzikos, C., & Paragios, N. (2013). Deformable medical image registration: A survey. IEEE transactions on medical imaging, 32(7), 1153-1190.

[68] Thirion, J. P. (1998). Image matching as a diffusion process: an analogy with Maxwell's demons. Medical image analysis, 2(3), 243-260.

[69] Liu, D., Hu, Z., Wang, G., & Sun, L. (2019). Sound transmission-based elastography imaging. IEEE Access, 7, 74383-74392.